EPRASHEED
signature series

2017 – Issue 48

Saudi Arabia oil & gas

www.saudiarabiaoilandgas.com

Inside

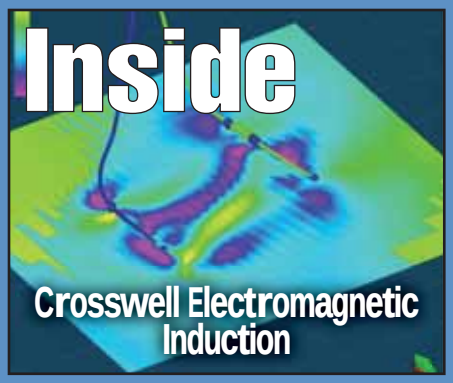

Crosswell Electromagnetic Induction

Sweep Efficiency in Horizontal Waterfloods

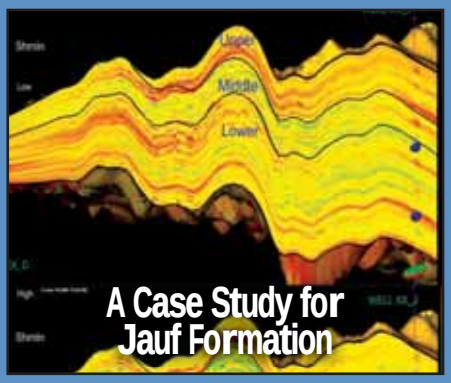

A Case Study for Jauf Formation

Optimize your plant for a safe, efficient start-up

Through our detailed engineering and expert field execution

When considering mechanical pre-commissioning and commissioning for your plant start-up – ***consider this.*** Innovative engineering and service excellence results in greater quality. ***And THAT reduces costs.*** We're an oil and gas services company committed to excellence. Everything we do in the field we engineer first to meet your specific needs.

Demand Professionals. Demand FourQuest Energy.

For a complete list of services, visit our website.

www.fourquest.com

Four Quest Energy

Connect with us on:

SCAN THIS CODE TO VIEW OUR WEBSITE

Optimize zone by zone.

Maximize production. Reduce costs. Save time.

UNRIVALED PERFORMANCE

45+ zones
fractured by the i-ball® frac sleeve in cemented and openhole wells in the Bakken play

FASTER DRILLOUT

97% composite
TruFrac™ plugs withstand up to 10,000 psi and 300°F

UNLIMITED HOLD

Full working pressure
with an unlimited hold period achieved during testing with the SMART toe sleeve

Every well—and every zone within each well—is an opportunity for production optimization. Our technologies provide extraordinary modularity and design flexibility, ensuring that each completion is the right answer for your budget and your formation.

We offer collaborative completion design and modeling services along with a comprehensive suite of stimulation tools, including mechanical and swellable packers, high-torque frac sleeves, and durable composite plugs.

Contact and collaborate with us at weatherford.com/zoneselect

Weatherford®

مدينة الملك عبدالعزيز
للعلوم والتقنية KACST

Oil and Gas Research Institute

Hydrocarbon resources (crude oil and gas) are the main source of world energy, and as the international demand increases, the technical challenges increase to meet that demand. Hydrocarbon production optimization at minimum cost and the need to serve the national petroleum industry has been the driving force behind the establishment of the Oil and Gas Research Institute (OGRI) at King Abdulaziz City for Science and Technology (KACST). OGRI is a governmental research and development entity. Its applied research activities concentrate on the upstream sector of the petroleum industry. Fields of interest cover most of the petroleum science and engineering aspects through four main divisions:

- Reservoir Characterization and Numerical Simulation,
- Drilling Engineering,
- Rock Mechanics,
- Production and Enhanced Recovery.

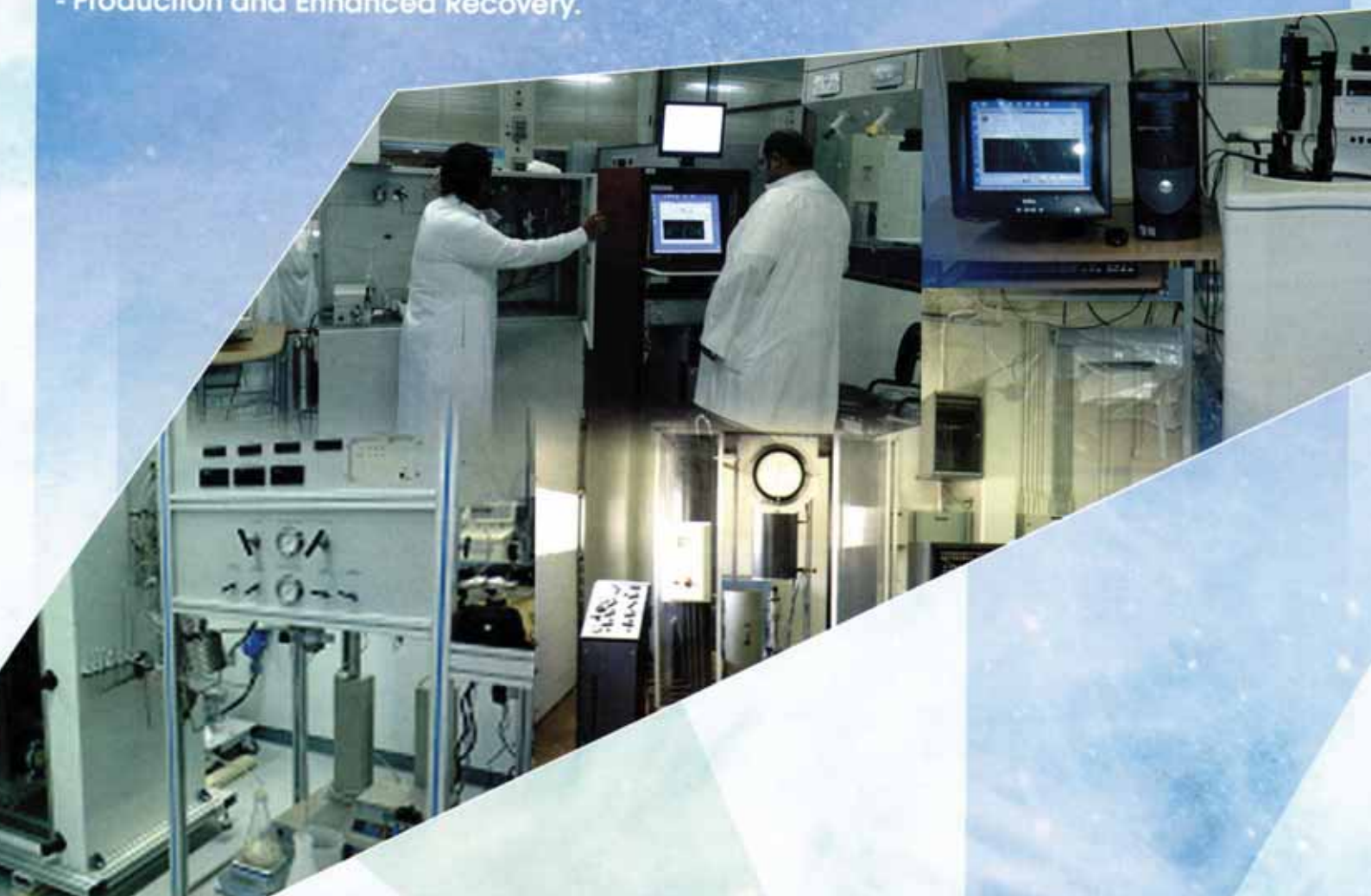

Services Provided

Service	Techniques
CONVENTIONAL CORE ANALYSIS	➤ Helium Porosity (Ambient Conditions) ➤ Gas Permeability & Porosity (Low and Reservoir Overburden Stress) ➤ Klinkenberg Correction ➤ Liquid Permeability (Reservoir Conditions)
SPECIAL CORE ANALYSIS (SCAL)	**CAPILLARY PRESSURE TESTS** ➤ Centrifuge Techniques (Reservoir Conditions) ➤ Low and High Pressure Mercury Injection and Withdrawal Technique ➤ Pore Size Distribution (PSD) **RELATIVE PERMEABILITY MEASUREMENTS** ➤ Unsteady State Flooding Technique (Reservoir Conditions) ➤ Centrifuge Technique (Reservoir Conditions) **WETTABILITY TESTS** ➤ Centrifuge USBM Method ➤ Contact angle Measurement (Ambient and Reservoir Conditions) ➤ Interfacial Tension Measurements **PETROGRAPHIC SERVICES** ➤ Sieve Analysis ➤ Particle Size Analysis ➤ Thin section
RESERVOIR FLUID ANALYSIS	➤ Interfacial & Surface tension ➤ Gas and Gas Condensate Viscosity ➤ Refractive index and pH ➤ Contact angle
ADVANCED RESERVOIR ENGINEERING	➤ Water-Oil /Water-Gas Displacement ➤ Gas Flooding and WAG ➤ Chemical Flooding
PETROLEUM RELATED ROCK MECHANICS	➤ Uniaxial, Triaxial, and Hydrostatic Compressive strength ➤ Stress-Strain Behavior ➤ Failure Envelope ➤ Elastic moduli ➤ Bulk and Pore Compressibility ➤ Fracture Toughness

OGRI - KACST - K.S.A - P.O. Box. 6086 Riyadh 11442
Tel. : +966 1 4813307 Fax : +966 1 4813526

EPRASHEED
signature series
2017 – Issue 48
Saudi Arabia oil & gas
Saudi Arabia Oil & Gas (Print) ISSN 2045-6670
www.saudiarabiaoilandgas.com
Saudi Arabia Oil & Gas (Online) ISSN 2045-6689

Contents

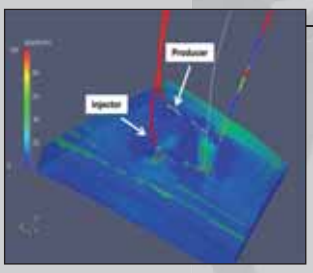

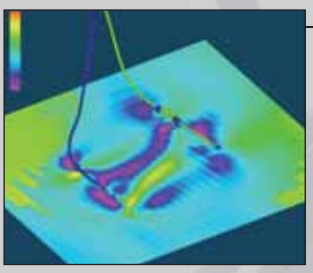

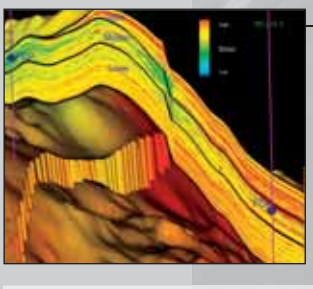

CEO and Founder
EPRasheed
Wajid Rasheed
wajid.rasheed@eprasheed.com
Editors
Majid Rasheed
Mauro Martins
Design
Sue Smith
sue.smith@eprasheed.com

United Kingdom
► Head Office
Tel: (44) 207 193 1602
► Adam Mehar
adam.mehar@saudiarabiaoilandgas.com
Main: (44) 1753 708872
Fax: (44) 1753 725460
Mobile: (44) 777 2096692

Saudi Arabia
► Akram ul Haq
PO BOX 3260, Jeddah 21471
akram.ul.haq@saudiarabiaoilandgas.com
Tel: (966) 557 276 426
► Mohanned AlSagri
mohanned.alsagri@saudiarabiaoilandgas.com

Brazil
► Ana Felix
afelix@braziloilandgas.com
Tel: (55) 21 9714 8690
► Fabio Jones
fabio.jones@braziloilandgas.com
Tel: (55) 21 9392 7821
► Roberto S. Zangrando
rzangrando@braziloilandgas.com
Tel: (55) 22 8818 8507

Manifa: An Environmental Success Story

DHAHRAN, January 4, 2017

For years, Saudi Aramco and King Fahd University of Petroleum and Minerals have worked together to protect the highly sensitive ecosystem in Manifa. A recent update session at the university shows that not only has the project maintained the integrity of the sensitive marine environment, it has actually enhanced it.

Innovative Planning

Senior management from Saudi Aramco recently gathered at the Center for Environment and Water at King Fahd University of Petroleum and Minerals (KFUPM) to get a current update of environmental achievements and long-term conservation projects on the company's flagship program for environmental stewardship.

Operational since 2013, the massive offshore Manifa field has a capacity to produce 900,000 barrels per day of Arabian Heavy crude oil, which allows the Kingdom to maintain its leading position as a global energy supplier. But what makes the Manifa project so important is the careful collaboration between Saudi Aramco engineers, Saudi Aramco Environmental Protection officials, and scientists to preserve the fragile ecosystem in Manifa Bay, which is famous as one of the top fish and shrimp nurseries on the Gulf Coast.

The result of that collaborative effort was an innovative plan to reach Manifa field – primarily located in shallow water – through building a world-class causeway, bridges, and laterals to connect the man-made islands. The computerized modeling of the 27 drilling islands, connected by a 42 kilometer causeway and 14 bridges to allow natural water circulation at Manifa Bay, has significantly contributed to enhance the natural flow of water, maintaining the bay as a perfect environment for shrimp and fish populations to grow.

During the design, construction, and dredging activities on the man-made islands, the Manifa mega-project as a whole followed strict environmental policies and standards in all aspects related to marine measures. This included the specific placement and configuration of causeway islands to avoid affecting the existing coral reefs, while meeting the requirements of drilling and oil production.

> During the design, construction, and dredging activities on the man-made islands, the Manifa mega-project as a whole followed strict environmental policies and standards in all aspects related to marine measures.

Celebrating a Success Story

At the KFUPM event hosted by Alaadin A. Bukhari of KFUPM's Center for Environment and Water, the Manifa program's achievements were celebrated with a number of presentations by Saudi Aramco and KFUPM experts. Scientists from the Marine Studies Section at KFUPM's Center for Environment and Water also presented MPD officials with its final report on the environmental impact of the project so far.

"Today, we celebrate and thank all of you who contributed to the landmark of the Manifa causeway," said Mohammed H. Al-Ghamdi, manager of the Manifa Producing Department (MPD). "Today, we can see the results. Since the construction of the causeway, marine life in Manifa has improved. Saudi Aramco's determination to protect the environment is not lip service; it is translated into action to affirm our determination toward the Manifa marine environment.

"This 10 years of partnership with the Saudi Aramco Environmental Protection Department (EPD) and King Fahd University of Petroleum and Minerals was established initially to protect the ecosystem through developing a creative causeway design and conducting a survey of the marine environment at Manifa Bay before and after the causeway construction," Al-Ghamdi added. "However, we did not stop there. Instead, we capitalized on this partnership to improve and increase the density of marine life."

The results of this careful collaboration is already paying off. In multiple reports, KFUPM scientists showed how the causeway design had not only maintained but also enhanced the natural circulation of tidal waters into and out of Manifa Bay.

Dissolved oxygen rates are higher than they were before construction, making those shallow waters a healthier environment for fish and shrimp larvae. Coral reefs have grown in size and seem to be spreading onto the rocks of the Manifa causeway itself. Seagrass meadows also have increased, covering 70% more area than before construction.

Far from destroying the fragile ecosystem in Manifa Bay, the Manifa causeway is showing signs of improving the habitat for the larval and juvenile shrimp and fish populations that call Manifa their home.

A Commitment to the Environment

For every presentation on environmental challenges, the 10-year trends in biodiversity at Manifa Bay, and Manifa's long history and future potential as a nursery ground for shrimp and fish, there was an open exchange of views in question and answer sessions. What was clear to all was that Saudi Aramco's commitment to preserving the marine environment at Manifa and other facilities was heartfelt and was a central corporate value, woven into every aspect of the way we do business.

> What was clear to all was that Saudi Aramco's commitment to preserving the marine environment at Manifa and other facilities was heartfelt and was a central corporate value, woven into every aspect of the way we do business.

While KFUPM scientists gave presentations and presented posters, showing specific data on Manifa Bay's recovery, post-construction, Aramco experts laid out the broader framework of the company's environmental stewardship, including future mitigation efforts.

Khaled A. Abdulkader, a senior consultant in EPD, gave a presentation about the three layers of monitoring for compliance with strict environmental regulations, and the host of mitigation efforts made by the company – including the construction of a new fishing port at the coastal town of Dareen.

Abdulkader says Saudi Aramco made many modifications to the Manifa project's design, including removing the northwestern portion of the causeway and building bridges in other parts of the causeway to increase tidal circulation; introducing the zero discharge of drilling wastes, through cutting reinjection and "skip and ship" to safer onshore locations; and the plantation of mangrove forests, construction of shrimp nurseries, and construction of artificial reefs to encourage marine life to quickly rebound after construction was complete.

The redesign of the causeway to encourage circulation was especially successful, Abdulkader said. Initial plans for a causeway would have slowed the "flush rate" of Manifa Bay to 71 days from the 17 day natural rate before construction. By opening up the bay with the causeway and bridge design, the flush rate was enhanced to 15 days. Today, monitoring data shows the actual flush rate is 11 days, much faster than the computer models had projected.

"Manifa is a highly productive marine ecosystem, and that makes the project very challenging," Abdulkader said. "It is good to get a chance to document all that was done to maintain a project as important as this is to the Kingdom's economy, and at the same time protect the ecosystem at Manifa."

Deep Reading Technology Integrated with Inflow Control Devices to Improve Sweep Efficiency in Horizontal Waterfloods

By H. Onur Balan, Anuj Gupta and Daniel T. Georgi, Aramco Research Center-Houston; Ali Alkhatib and Alberto Marsala, Saudi Aramco.

This paper was prepared for presentation at the Abu Dhabi International Petroleum Exhibition and Conference held in Abu Dhabi, UAE, 7–10 November 2016.

Abstract

Premature breakthrough and low sweep efficiency during waterfloods result from heterogeneity in the permeability field in a reservoir. Production wells with inflow control valves/inflow control devices (ICVs/ICDs) have the ability to reduce the water-oil ratio by shutting in flow ports with high water cut. Subsequently, this technology has been limited to a response based on detection of water breakthrough at production wells. Deep reading technologies have been reported to be successful in detecting the approaching waterfront before its breakthrough. The objective of this study is to investigate if the technology for early front detection combined with ICVs/ICDs can improve sweep efficiency in horizontal waterfloods.

In this study, a synthetic horizontal well pair model is built using a black oil reservoir simulator to study performance of waterflooding in a single layer heterogeneous oil reservoir and to understand the value of information obtained from deep reading technology to control ICVs/ICDs for optimizing waterfloods. The simulation results show that using ICVs/ICDs at the horizontal production well significantly improves sweep efficiency and reduces water production. Early detection of waterfront with deep reading technologies provides incremental oil recovery. An optimum location for waterfront detection exists between the injector and the producer to improve oil production with specified injection and production constraints. Deep reading technologies may also provide valuable information about the mobility field between the well pair to reduce uncertainty in heterogeneity, which can be used to update the geological model for better history matching and forecasting production.

Introduction

In recent years, the technology to detect water injection fronts (Marsala et al. 2011, 2013; Dutta et al. 2011) and conformance control with inflow control valves/inflow control devices (ICVs/ICDs) had a tremendous development in the industry. A cross-well electromagnetic field survey was recently deployed in Saudi Arabia between two horizontal wells, spaced at more than 1.3 km, imaging fluid distribution in a carbonate reservoir between a water injector and an oil producer (Marsala et al. 2015). The results from this survey clearly indicated how the injected water is confined in highly fractured corridors, leaving unswept volumes in the tighter and less permeable layers of the

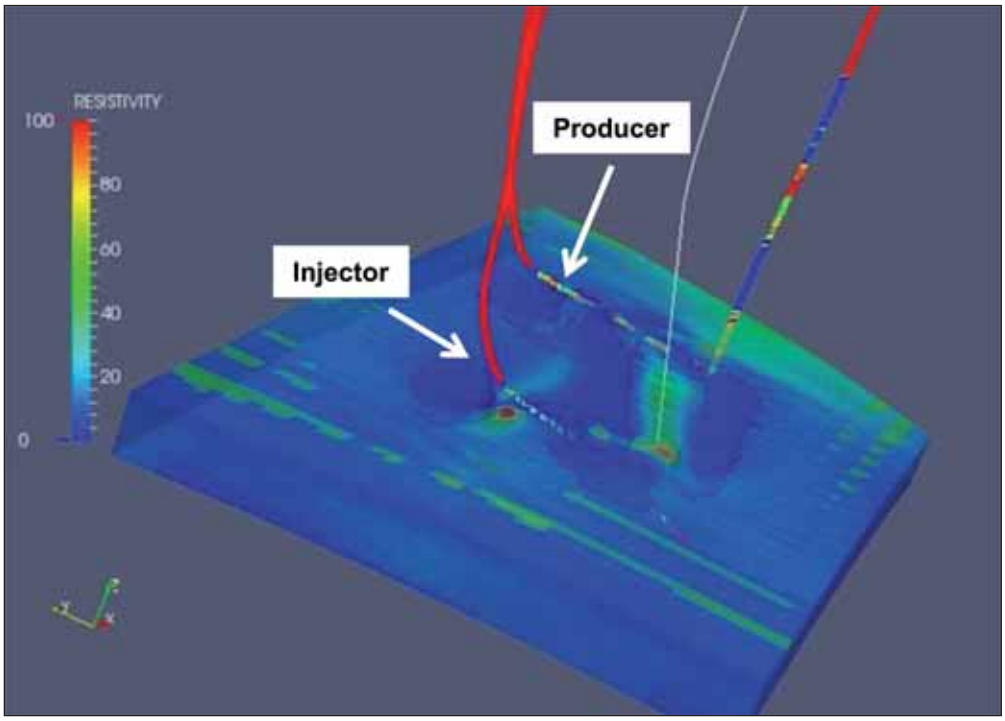

Fig. 1. 3D resistivity inversion cube from a cross-well electromagnetic survey between a water injector and a watered out oil producer horizontal wells, spaced 1.3 km (Marsala et al. 2015). Dark blue zones (less than 2 ohm.m) represent reservoir volumes swept by the injected water. The water injection front is clearly not uniform in this case of relatively tight matrix carbonate reservoir with highly conductive fracture corridors. A newly drilled slanted well in the interwell area (white trajectory) targeted an unswept zone of the reservoir.

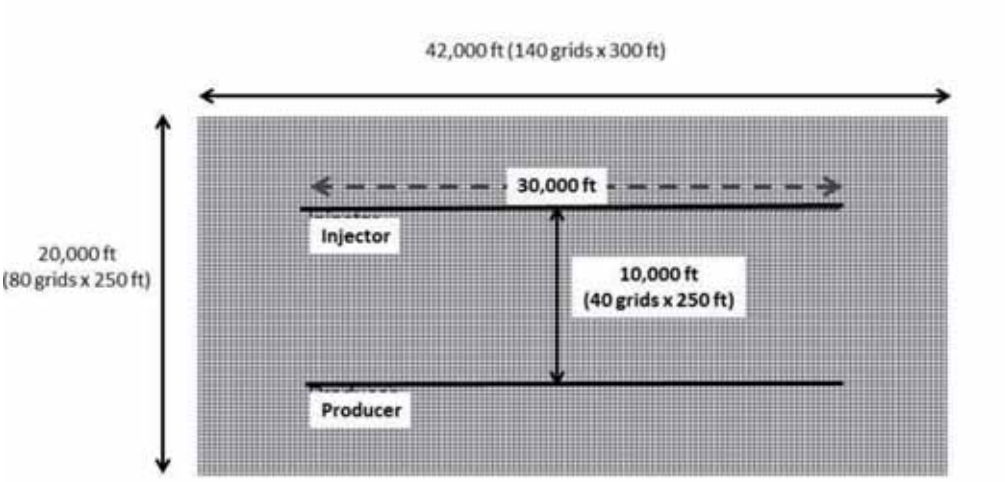

Fig. 2. A single layer simulation model for horizontal waterflooding.

interwell volumes of the reservoir, Fig. 1. Field data and simulation studies (Aakre et al. 2014; Al-Kadem et al. 2015; Eltaher et al. 2014; Halvorsen et al. 2016; Iqbal et al. 2015; Mathiesen et al. 2014; Stone et al. 2015; Thornton et al. 2012) indicate that using ICVs/ICDs to solve conformance control issues such as gas-water coning is beneficial. In all these studies, ICVs/ICDs react after the breakthrough of water-gas at production wells. Subsequently, the value of controlling ICVs/ICDs based on early front detection technology is not fully understood and as a result there is reluctance on the part of operating companies to invest in them. In this study, the objective is to investigate if the technology for early front detection combined with ICVs/ICDs can help to improve sweep efficiency and reduce the water-to-oil ratio in horizontal waterfloods.

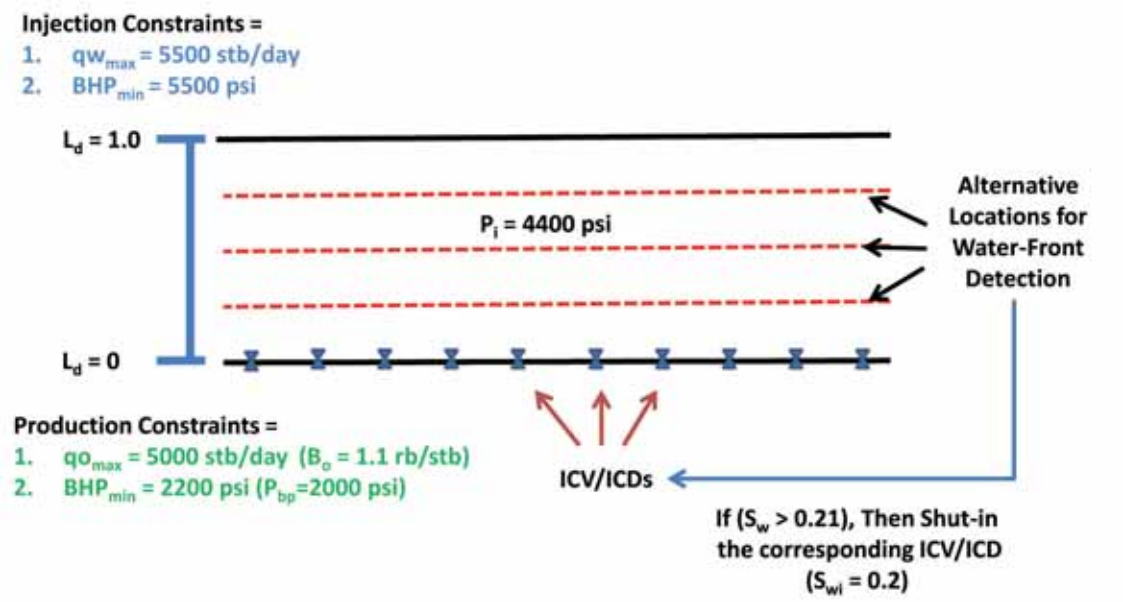

Fig. 3. A schematic showing alternative locations for waterfront detection between the horizontal wells.

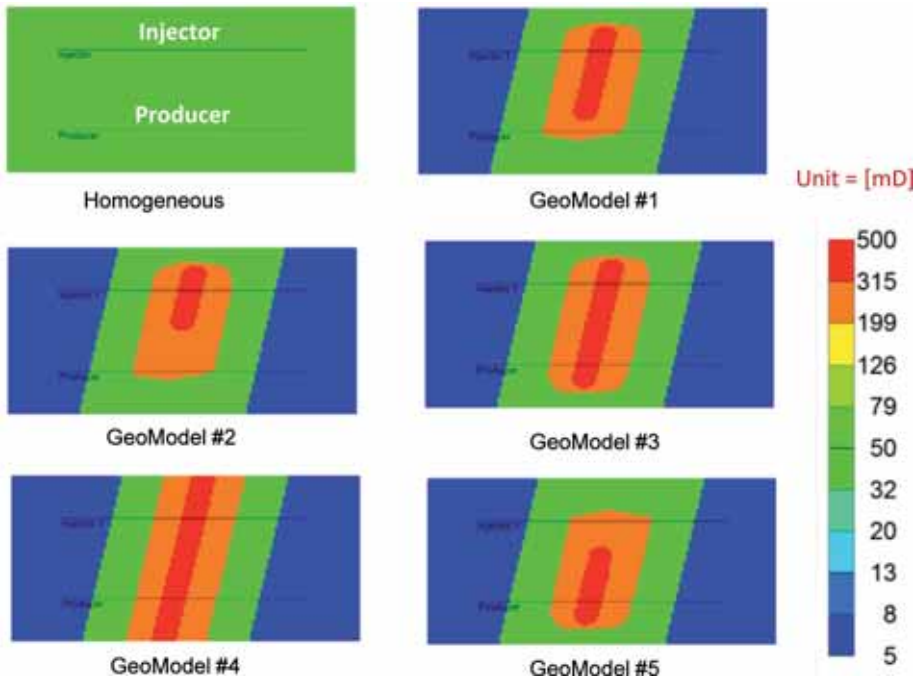

Fig. 4. Synthetic geomodels with different heterogeneity in permeability field.

Methodology

In this study, a single layer simulation model (140 × 80 grids) with two horizontal wells, Fig. 2, is built to simulate waterflooding using a black oil reservoir simulator (CMG IMEX). The length of both wells and the well spacing are 30,000 ft and 10,000 ft, respectively. Since this is a single layer model, the gravity segregation is ignored and areal sweep efficiency is used as an indicator of increased recovery.

Initial reservoir pressure is set to 4,400 psi, Fig. 3. Connate water saturation, which is equal to irreducible water saturation, is 0.2. Water is injected at a constant rate of 5,500 bbl/day and at a maximum bottom-hole pressure (BHP) of 5,500 psi. Oil is produced at a constant rate of 5,000 bbl/day (oil formation volume factor = 1.1 rb/stb), which ensures voidage replacement. Bubble point pressure is set to 2,000 psi. Minimum BHP assigned for the producer is 2,200 psi to prevent

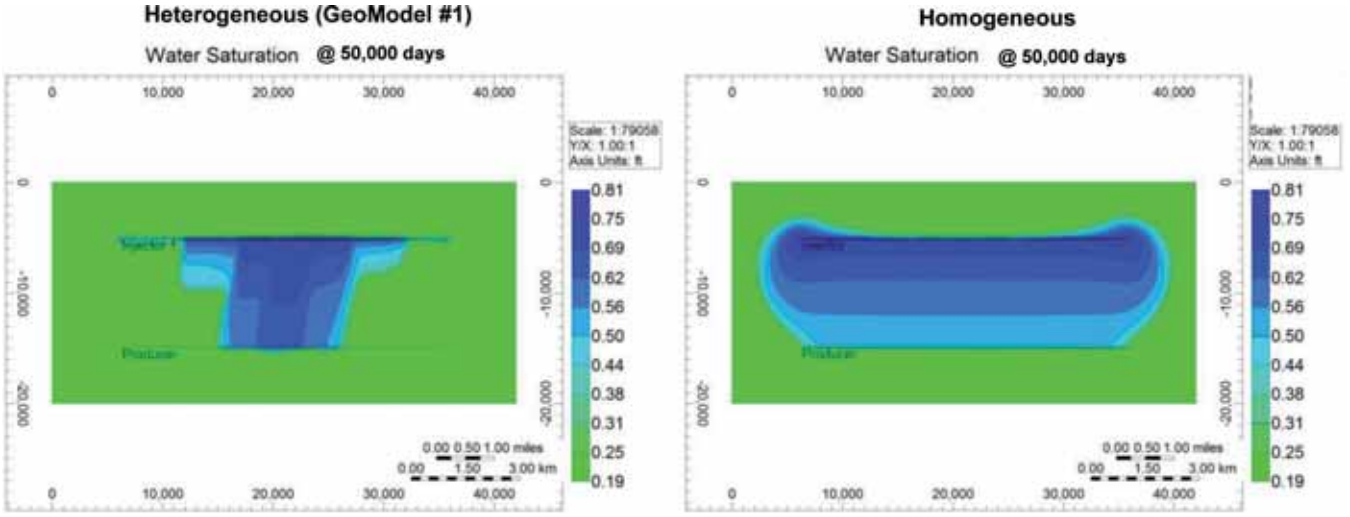

Fig. 5. Water saturation maps for heterogeneous (left) and homogeneous (right) cases after 50,000 days of waterflooding. Sweep efficiency is significantly reduced by heterogeneity in a permeability field. Water prefers to flow through the least resistant pathway from injector to producer.

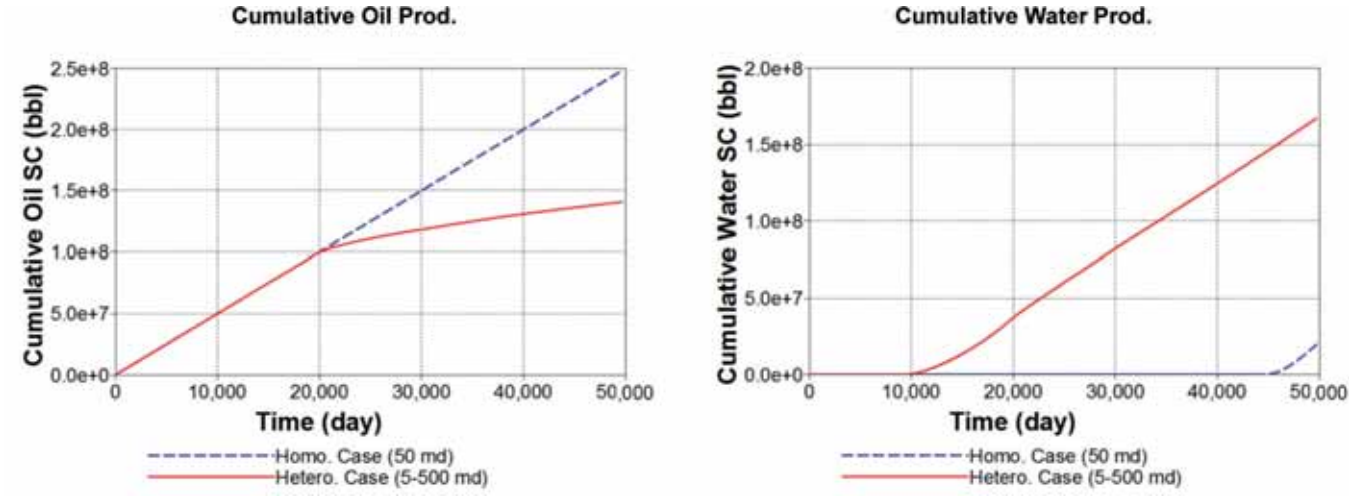

Fig. 6. Heterogeneity in a permeability field leads to lower oil recovery (left) and higher water production with early breakthrough (right).

free gas generation around the producer. Independently acting ICVs/ICDs are assigned for each perforation on the horizontal producer. If the waterfront is detected at the production well, an ICV/ICD is shut in when water cut at the corresponding perforation is larger than 10%. If the waterfront is detected at a distance from the production well, then the ICV/ICD is shut in when water saturation in the assigned distant grid is larger than 0.2. Although these constraints seem to be very conservative, the simulation results will provide an idea about the maximum benefit obtained from using deep reading technology and ICVs/ICDs together.

Figure 3 also shows the alternative locations for waterfront detection are considered to find the optimum location between the wells to maximize oil production with ICVs/ICDs. Moreover, different synthetic geomodels are built to investigate the effect of heterogeneity in the permeability field on oil recovery, water production and breakthrough, Fig. 4. All simulations are run for 50,000 days.

Results and Discussion

The Effect of Heterogeneity in Permeability Field

Water displaces oil more uniformly in a homogeneous case than it does in a heterogeneous case, Fig. 5. Water phase prefers to flow through the least resistant pathway from injector to producer. Therefore, water breakthrough for a heterogeneous case occurs much earlier than that for a homogeneous case, Fig. 6. This results in lower areal sweep efficiency, Fig. 5, and 40% lower oil recovery in the heterogeneous case.

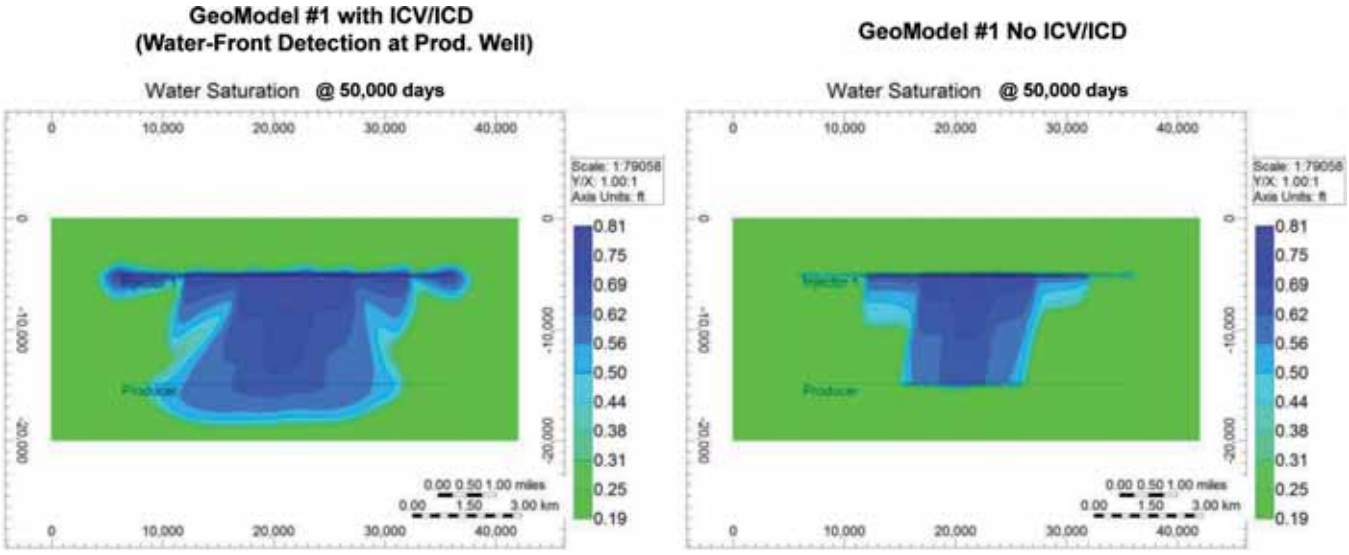

Fig. 7. Water saturation maps after 50,000 days of waterflooding with (left) and without (right) ICV/ICD (Geomodel #1) cases. Using ICVs/ICDs at the production well improves sweep efficiency. Each ICV/ICD is shut in independently if water cut is larger than 10%.

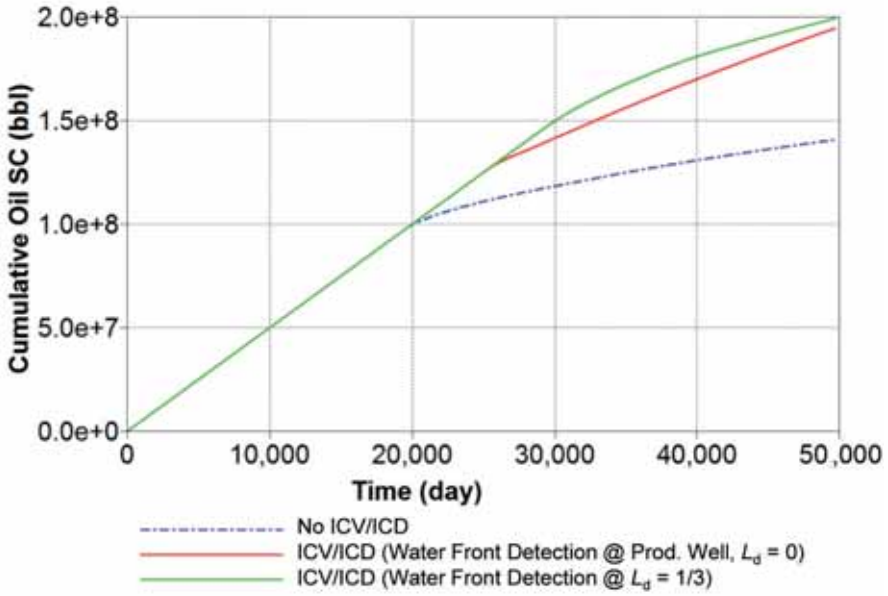

Fig. 8. Using ICVs/ICDs with waterfront detection at the production well improves oil recovery by increasing sweep efficiency. Furthermore, detection of the waterfront away from the production well results in an incremental oil recovery.

The effect of heterogeneity is expected and it could be more pronounced given the uncertainty in reservoir characterization. When applying such a workflow to a real reservoir model, this would require considering multiple history matched permeability realizations to produce representative results with respect to the effect of uncertainty in heterogeneity.

The Effect of Using ICVs/ICDs

Using ICVs/ICDs at the production well improves areal sweep efficiency significantly, Fig. 7. For this case, waterfront is detected at the production well, i.e., the ICV/ICD is shut in if the flowing stream exceeds 10% water cut. This helps to divert water from high permeability to low permeability regions. Improved sweep efficiency results in higher oil production and lower water production with delayed breakthrough.

Using ICVs/ICDs with Deep Reading Technology

In the previous section, water is detected after its breakthrough. In this section, however, two different scenarios are simulated to show the effect of pre-

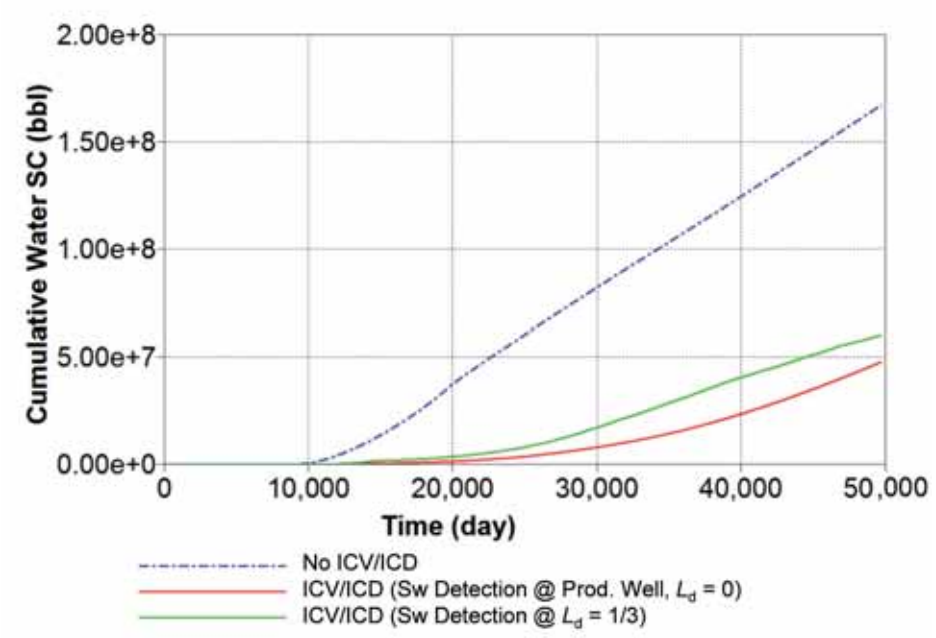

Fig. 9. Using ICVs/ICDs with waterfront detection at the production well delays water breakthrough and reduces water production. There is no additional benefit of detecting the waterfront earlier on water production; however, cumulative water production is still much lower than the no ICV/ICD case.

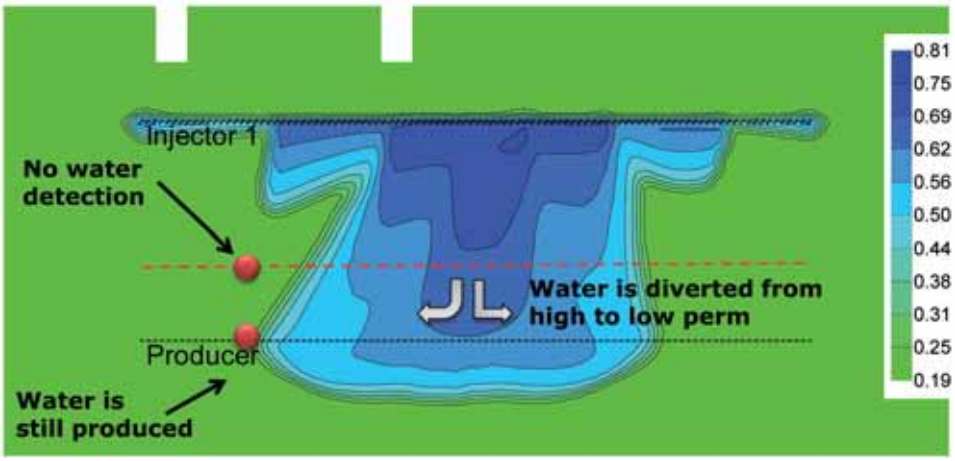

Fig. 10. At certain ICVs/ICDs water production is still continued even after its breakthrough, since no waterfront is detected at a distance from the production well due to diversion of water from high- to low-permeability regions.

breakthrough detection of waterfront on oil and water production, Figs. 8 and 9. Ld is defined as dimensionless distance between the injector and the producer, Fig. 3, which ranges from zero at the producer to 1 at the injector. If L_d = 0, then waterfront is detected at the production well. If L_d = 1/3, then it is detected at a distance of one-third of the well spacing from the producer. The results show that oil recovery increases if the ICVs/ICDs are closed, based on earlier waterfront detection, Fig. 8. Subsequently, increased oil production is accompanied by a slight increase in water production, Fig. 9, which may result from heterogeneity in the permeability field and the formulation of the problem. As ICVs/ICDs are closed due to early detection of the waterfront, injected water is diverted from high- to low-permeability regions, Fig. 10. At some ICVs/ICDs, however, water production is continued even after its breakthrough, since no waterfront is detected at a distance from the production well due to diversion. As a result, those ICVs/ICDs are not triggered to shut in.

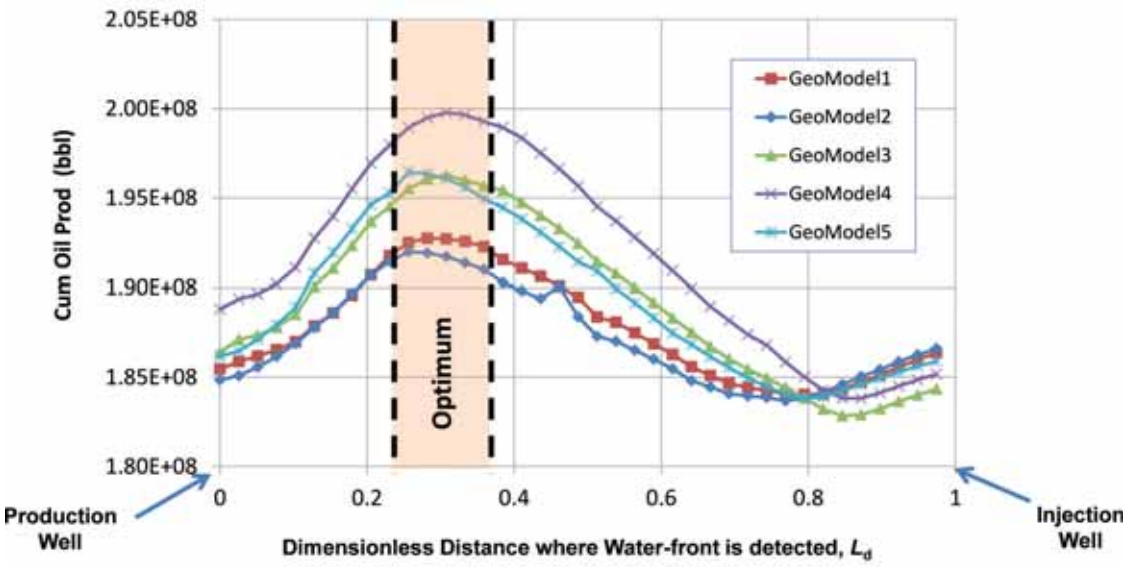

Fig. 11. An optimum location for early waterfront detection exists between the injector and the producer to improve oil production at the specified injection and production constraints.

Optimum Location for Early Waterfront Detection

In this section, we search for the optimum location for early waterfront detection, $(L_d)_{opt}$ between the horizontal injector and producer to maximize oil production with ICVs/ICDs. Five different synthetic geomodels, Fig. 4, are used in the simulations to show the effect of different heterogeneity in the permeability field on the optimum location. It is found that $(L_d)_{opt}$ ranges from 0.25 to 0.35 regardless of the geomodels used in this study, Fig. 11.

Future work will focus on incorporating the effects of gravity and uncertainty in heterogeneity by using multiple realizations of real geological models on the performance of this workflow to recommend more robust reservoir management policies. This will include the effects of reservoir parameters controlling mobility and will consider a number of uncertainty quantification methods such as the probabilistic collocation method (Alkhatib and King 2014; Saif et al. 2016) and the multilevel Monte Carlo method (Alkhatib and Babaei 2016).

Conclusions

In recent years, the oil industry witnessed tremendous development of deep reading technologies and the availability of ICDs. In this simulation study, benefits of proactively controlling ICVs/ICDs based on early front detection technology have been investigated to improve sweep efficiency and reduce water production in horizontal waterfloods.

The major conclusions drawn are:

- Using ICVs/ICDs at the horizontal production well significantly improves sweep efficiency and reduces water production.
- Early detection of waterfront with deep reading technology provides incremental oil recovery.
- An optimum location for early waterfront detection exists between the injector and the producer to improve oil production at the specified injection and production constraints.
- Deep reading technology may also provide valuable information about mobility of the field, which can be used to reduce uncertainty in geological models for better history matching and production forecasting.

Nomenclature

$(qo)_{max}$ = maximum oil production rate, stb/d
BHP_{min} = minimum bottomhole pressure, psia
$(q_w)_{max}$ = maximum water production rate, stb/d
P_i = initial reservoir pressure, psi
S_w = water saturation, fraction
S_{wi}= initial water saturation, fraction
L_d = dimensionless distance between injector and producer
$(Ld)_{opt}$ = dimensionless optimum location between injector and producer

Acknowledgment

We acknowledge Saudi Aramco and Aramco Services Company for the permission to publish this paper and to all the colleagues who made this work possible.

References

Aakre, H., Halvorsen, B. and Werswick, B. et al. 2014. Autonomous Inflow Control Valve for Heavy and Extra-Heavy Oil. Paper SPE 171141 presented at the SPE Heavy and Extra Heavy Oil Conference – Latin America, Medellin, Colombia, 24-26 September.

Alkhatib, A. and King, P. 2014. Robust Quantification of Parametric Uncertainty for Surfactant-Polymer Flooding. Journal of Computational Geosciences, 18(1): 77-101.

Alkhatib, A. and Babaei, M. 2016. Applying the Multilevel Monte Carlo Method for Heterogeneity-Induced Uncertainty Quantification of Surfactant/Polymer Flooding. SPE Journal, 21(4): 1192-1203.

Al-Kadem, M., Al-Muhaish, A. and Lee, B.O. et al. 2015. First Autonomous ICD Installation in Saudi Arabia – Modeling a Field Case. Paper SPE 177977 presented at the SPE Saudi Arabia Section Annual Technical Symposium and Exhibition, al-Khobar, Saudi Arabia, 21-23 April.

Dutta, S.M., Reiderman, A. and Schoonover, L.G. et al. 2011. Novel Borehole System for Reservoir Monitoring Using Transient Electromagnetics. Paper SPE 142510 presented at the SPE Middle East Oil and Gas Show and Conference, Manama, Bahrain, 25-28 September.

Eltaher, E., Muradov, K. and Dacies, D. et al. 2014. Autonomous Inflow Control Valves – their Modeling and "Added Value." Paper SPE 170780 presented at the SPE Annual Technical Conference and Exhibition, Amsterdam, the Netherlands, 27-29 October.

Halvorsen, M., Madsen, M. and Vikøren M. et al. 2016. Enhanced Oil Recovery on Troll Field by Implementing Autonomous Inflow Control Device. Paper SPE 180037 presented at the SPE Bergen One Day Seminar, Bergen, Norway, 20 April.

Iqbal, F., Iskandar, R. and Abbas, H.A. et al. 2015. Autonomous Inflow Control Device – A Case Study of First Successful Field Trial in GCC for Water Conformance. Paper SPE presented at the Abu Dhabi International Petroleum Exhibition and Conference, Abu Dhabi, UAE, 9-12 November.

Marsala, A.F., Al-Buali, M. and Ali, Z. et al. 2011. First Borehole to Surface Electromagnetic Survey in KSA: Reservoir Mapping & Monitoring at a New Scale. Paper SPE 146348-PP presented at the SPE Annual Technical Conference and Exhibition, Denver, Colorado, 30 October – 2 November.

Marsala, A.F., Lyngra, S. and Widjaja, D.R. et al. 2013. Fluid Distribution Inter-Well Mapping in Multiple Reservoirs by Innovative Borehole to Surface Electromagnetic: Survey Design and Field Acquisition. Paper IPTC-17045-MS presented at the International Petroleum Technology Conference, Beijing, China, 26-28 March.

Marsala, A.F., Lyngra, S. and Safdar, M. et al. 2015. Crosswell Electromagnetic Induction between Two Widely Spaced Horizontal Wells: Coiled Tubing Conveyed Data Collection and 3D Inversion from a Carbonate Reservoir in Saudi Arabia. 85th Annual International Meeting, SEG Expanded Abstracts.

Mathiesen, V., Werswick, B. and Aakre, H. 2014. The Next Generation Inflow Control, the Next Step to Increase Oil Recovery on the Norwegian Continental Shelf. Paper SPE 169233 presented at the SPE Bergen One Day Seminar, Bergen, Norway, 2 April.

Saif S.F., Alkhatib A.M. and Marsala, A.F. 2016. Enhanced Petrophysical Interpretation of 3D Electromagnetic Surveys for Reservoir Characterization. Paper SPE 182768 presented at the SPE Saudi Arabia Annual Technical Symposium and Exhibition, al-Khobar, Saudi Arabia, 25 April.

Stone, T.W., Moen, T. and Edwards, D.A. et al. 2015. Optimized Design of Autonomous Control Devices for Gas and Water Coning. Paper SPE 173203 presented at the SPE Reservoir Simulation Symposium, Houston, Texas, 23-25 February.

Thornton, K., Jorquera, R. and Soliman, M.Y. 2012. Optimization of Inflow Control Device Placement and Mechanical Conformance Decisions Using a New Coupled Well Intervention Simulator. Paper SPE 162471 presented at the Abu Dhabi International Petroleum Exhibition and Conference, Abu Dhabi, UAE, 11-12 November.

Crosswell Electromagnetic Induction Between Two Widely Spaced Horizontal Wells: Coiled-Tubing Conveyed Data Collection and 3D Inversion from a Carbonate Reservoir in Saudi Arabia

By Alberto F. Marsala*, and Stig Lyngra, Saudi Aramco; Muhammad Safdar, Ping Zhang and Michael Wilt, Schlumberger.

Summary

This paper describes the results of a crosswell electromagnetic (known also as DeepLook EM) induction survey between two widely spaced horizontal wells with associated 3D inversion results. The project was designed to map oil and water saturations in a naturally fractured reservoir located in Saudi Arabia. The survey was conducted between a ~ 1 kilometer (km) long horizontal water injector and a ~1 km long horizontal producer. The two wellbores are drilled at an average distance of 1.3 km apart in the reservoir. The coiled-tubing (CT) deployed system operated at a very low noise resulting in an extremely high-quality data set. 3D inversion yielded a resistivity distribution consistent with large volumes of swept reservoir within fracture corridors. The inversion also revealed significant unswept reservoir volume in between the wells. The described survey is the first of its kind in the industry.

Introduction

Crosswell electromagnetic (EM) was initially developed in the 1990s. The initial technology application involves applying inductive physics and vertical well 2D inversion to interrogate the inter-well resistivity distribution. The method has since developed into a mature oil and gas technology, especially for enhanced oil recovery (EOR) projects and time-lapse studies (Wilt et al. 1995). Applying the technology to horizontal wells involves an entirely new set of challenges. When the wells are oriented horizontally, the sensors are sensitive to both vertical and horizontal variations, transposing the inversion into a 3D problem. As the measurements are confined to a limited number of vertical levels, the problem is extremely undetermined; i.e., there are far fewer observations than required to determine the resistivity of all the individual voxels. An additional complication is that standard wireline deployment of tools is not possible in horizontal wells. Since coiled tubing (CT) or tractor tool deployment is required, the survey time requirement and cost are significantly higher than for the vertical EM application.

The study is part of a larger Saudi Aramco Research and Development (R&D) effort to understand the saturation distribution in fracture controlled reservoirs and to help devise strategies for improved production and recovery. The reported project follows on a previous crosswell EM study in which a similar technology was applied to vertical wells to study matrix saturation using 2D workflows (Marsala et al. 2008 and Malalla et al. 2009).

The results of a field survey, acquired between two widely spaced horizontal wells in a fractured carbonate

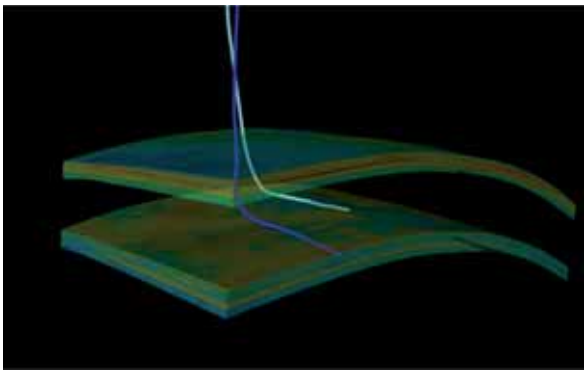

Fig. 1: The two carbonate oil reservoirs and the producer (green)/injector (blue) pair used for the crosswell EM deployment.

reservoir in Saudi Arabia, are described. We propose a methodology to obtain useful 3D inversions of a significantly underdetermined problem and describe the initial inversion results. A detailed analysis of the inversion process is presented in Marsala, et al. (2015).

Field Setting

The survey was acquired in a giant mature oil field in Saudi Arabia with two primary reservoirs. Production from the Upper carbonate reservoir began in 1946, and water flooding was initiated in the mid-1950s (Lyngra et al. 2015). In the southern part of the field, a separate Lower reservoir is located 150 m beneath the Upper reservoir. The Lower reservoir has ample present-day remaining oil volumes. The horizontal producer/injector pair are both completed in the Lower reservoir, as shown in Figure 1.

The Lower reservoir is approximately 100 m thick and has a similar porosity to the overlying Upper reservoir but significantly lower matrix permeability. The Upper and Lower reservoirs are known to be connected via a clustered fracture network, or fracture corridors. The reservoir pressures for the two reservoirs have tracked each other throughout the field history, which clearly demonstrates clear evidence of inter-reservoir communication. The Lower reservoir production and recovery behavior is fracture dominated with preferential water flow along large-scale fracture networks, which results in a large matrix block with less fracture intensity being left unswept (Lyngra et al., 2015). Moreover, these Lower reservoir inter well matrix blocks are difficult to identify based on well data alone, which is the primary justification for the R&D expenditures on developing suitable inter well hydrocarbon mapping techniques. EM is currently the most advanced inter well hydrocarbon mapping technology deployed in the Lower reservoir.

Well Screening and Pre-survey Feasibility Studies

All relevant Lower reservoir wells in the target oil field were carefully screened for well spacing. As this survey was the first in the industry between two horizontal wells, it was not expected that the EM detection distance would be much beyond 1 km. The existence of one or more inter well large fracture corridor(s) within the survey area was also considered important for the initial field application. The Lower reservoir near-vertical large-scale fracture events have often been seen to cause uneven water advancement with sweep predominantly taking place in the near vicinity of the events. The swept area has typically been seen to be <100 m on each side of the fracture corridor. A horizontal crosswell survey with this type of event within the survey area is expected to have considerable resistivity contrasts, which should be distinguishable as swept/unswept areas in the post-survey inversion of the acquired data.

The screening process resulted in the injector/producer pair, previously presented in Figure 1, being selected. These two horizontal wells were drilled roughly parallel, approximately 1.3 km apart, although the two wells penetrate different levels within the Lower reservoir. The injector was drilled as a high-angle slant well penetrating the full reservoir section and completed open hole over its entire 1 km length. Production logs run in this injector indicated most of the injected water exited the wellbore through an extensive fracture corridor encountered within the initial 100 m of the open hole. The producer

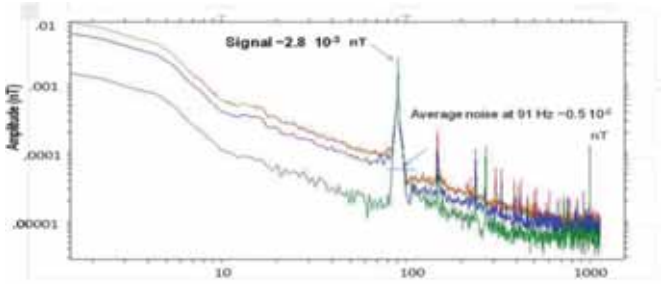

Fig 2: Crosswell EM spectrum for open-open section.

was drilled as a true horizontal well penetrating only the top portion of the reservoir. The well was also initially completed as a 1 km open hole completion. A water-bearing major fracture corridor was penetrated during drilling at the heel of the open hole. The producer was tested after completion, and it produced mainly water. The initial 350 m of the open hole was later cased off with a steel liner to eliminate the water production from the fracture zones crossed near the heel of the well. After the work over, the producer initially produced water free at a high oil rate, but after a gradual rise in water cut, the well ceased flowing approximately one year prior to running the EM survey due to well lift issues associated with the high water cut. The primary purpose of the presented survey is to perform a tomographic imaging between the two wells to identify unswept oil volumes that can be targeted by future wells.

Prior to field deployment, feasibility simulations were made to determine the ability of the crosswell EM technology to: 1) record signals between horizontal wells spaced more than 1 km apart; 2) map inter well fracture corridors as the primary target within the proposed survey area. Pre-job feasibility work was also performed to ensure that the existing wireline tools could be safely conveyed in CT through repeated logging runs.

The pre-survey feasibility study results were mixed. It was quickly determined that the tools were rigid enough for CT deployment. Also, it was projected that the 3D inversions could provide useful images of fracture corridors, if the corridors were more than 50 m wide and the background resistivity could be constrained and fixed during the inversion. The receiver signal level was identified as a concern at the 1.3-km well spacing. It was expected that large averaging times and limited sampling points would be required to sustain adequate signal-to-noise ratio (S/N) for the survey.

Crosswell EM Field Survey

The field deployment began in 2014 with the collection of CT-conveyed wireline logs in both wells. The open hole logs included: pulsed neutron to assess saturation along the wellbore profile, image logs for fracture imaging, dielectric, magnetic resonance for porosity determination, induction resistivity, and production logs for flow-zone identification.

After CT logging acquisition, both of the wells were injected with killing fluids. In April 2014, the crosswell data were collected by CT conveyance during a six day period. The transmitter and the receiver assemblies used a transmitter frequency of 91 Hz. It was quickly observed that the S/N was unusually high due to a very low noise level at the four receivers (Figure 2). With a data stack of 100, a noise level of 0.5 × 10-5 nT was obtained, which is more than 10 times lower than the lowest observed noise in vertical wells.

Different behaviors of the four receivers (Figure 2) were detected. This behavior has not been observed in earlier measurements due to much higher noise levels in vertical surveys. This suggests different noise sensitivities between the individual receivers.

This was the lowest noise ever recorded with a crosswell EM system. It is suspected that the low noise may be due to the lack of tension-induced vibration on the horizontally deployed sensors. An S/N of more than 50 dB was routinely measured in the open hole section

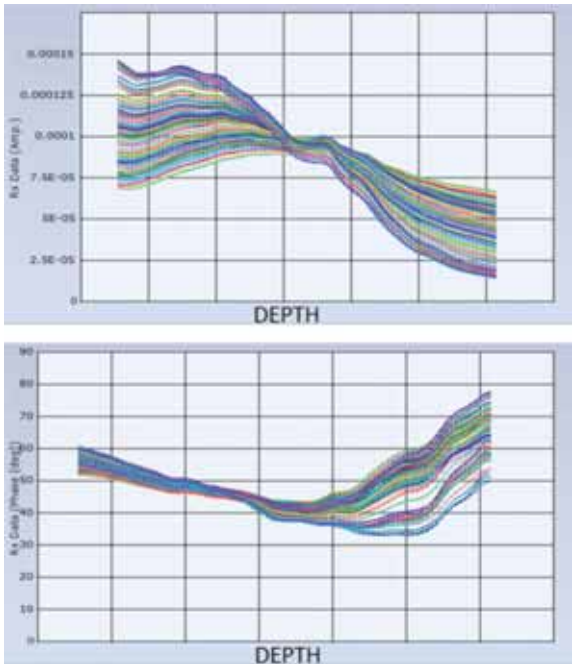

Fig 3: Amplitude and phase for open-open hole section.

and 33 dB in the lower-signal cased-hole section. The high S/N enabled logging the 1 km well at high logging speeds of 400 to 500m/h and still maintain excellent data quality at maximum sensor spacing of more than 1.6 km. This resulted in a 1-km-long profile collected for each four station (18 m) receiver gathers every 2.5 to 3 hours during field operation.

The data quality was very high and repeated profiles matched within 0.5%. Most of the logging time was spent in the 650 m producer open hole section, where receiver stations were positioned every 4.5 m. In total, more than 120 open hole profiles were collected, each 1km long and sampled at 4.5 m increments. In the cased-hole section, only 16 profiles were collected, spaced at 80 m intervals. The limited number of profiles was a result of concerns from the CT crew on the coil wear combined with an operational requirement to restore the injector well injection operation.

The open hole receiver amplitude/phase raw data gathers shows a remarkably smooth data set, Figure 3. In total, the data consisted of more than 12,000 measurements, of which 10,000 were in the open hole sections.

Data Processing and Interpretation

Field data were interpreted with a 3D finite difference inversion code (Mackie and Rodi, 2008). The workflow first assembles available logs and seismic data into a digital geologic model and then constructs a 3D resistivity volume from these data that is used as a starting guess for subsequent inversion.

In general, a 3D inversion of data collected in a single well pair is severely underdetermined for even a simple 3D model. The number of voxels is much larger than the number of data points and the distribution of measurements insufficient to resolve a 3D problem. On this basis, the inversion expectations should be low.

In this case, there are two conditions to make the 3D inversion more meaningful. First, the target reservoir is a low resistivity volume confined by thicker high resistivity (low porosity) layers, i.e., the induced signal is almost fully confined in the reservoir volume within well-defined upper and lower boundaries. Second, the sensors are oriented horizontally, which make them better able to image vertically oriented features, e.g., fracture corridors.

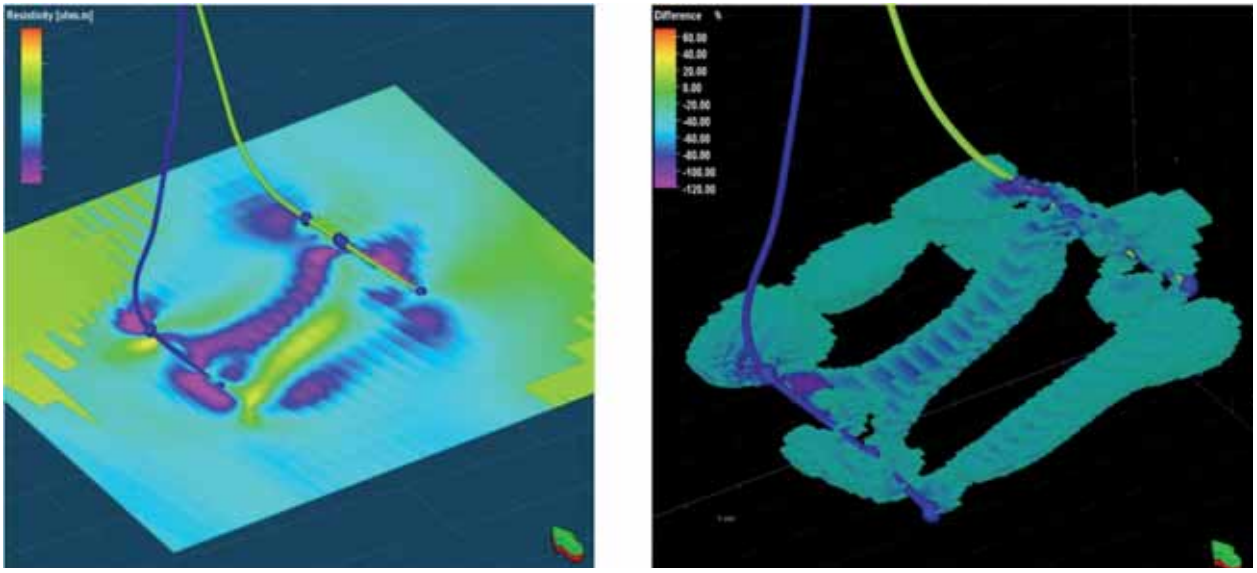

Fig 4a: 3D resistivity distribution at the midpoint of the Lower reservoir (left).
Fig 4b: Difference % image (right). Image volume depicts resistivity decreases of 35% or greater, relative to the resistivity starting model (well logs interpolation).
The injector is marked as blue and the producer as green.

Due to the background structure sensitivity, the data ware interpreted in two phases. Initially, the data ware fitted using a smooth background starting model with no constraints. This inversion fits the data very well, but showed some artifacts, which were mainly a function of a poor understanding of the background, i.e., the input for the formations above, below and outside the reservoir area of interest. After adjusting the background, the data ware re- inverted and fitted within 5%. After this run, the background structure was fixed for subsequent inversions. The remaining cells, within the reservoir, were allowed to adjust to fit the data. The inversion was not forced to honor the resistivity at the wells based on an argument that the measurements may not be representative of the 20m cells adjacent to the wells. The final inversion produced an overall <1% data misfit and a reasonable reservoir model.

The inversion results are presented in two maps, Figure 4a and 4b. Figure 4a presents the resistivity values within the reservoir extracting a 2D section from the 3D inversion cube, roughly at the midpoint of the Lower reservoir. Figure 4b shows the difference between the final model parameters and the initial values, i.e., it shows the inversion model adjustments required to fit the data.

Resistivity values within the reservoir ranged from 1 ohm- m (or less) for the fully swept zones to more than 30 ohm- m for unswept regions, Figure 4a. Low resistivity volumes are concentrated near the injector, near the producer and in three wide zones that connect the two wells.

The lowest resistivity values are adjacent to the injector corresponding to volumes in the reservoir section below the oil/water contact. It should be noted that these values are less than 1 ohm-m, corresponding to the original high salinity connate water, not the lower salinity injected water. This is also consistent with injection logs that show most of the low salinity injection water were injected into the fracture corridor at the heel.

Figure 4a also shows that the resistivity to be low adjacent to the producer. Fairly large volumes with a resistivity of 1 ohm-m or less are observed, which is consistent with recent logs and high water cut from this well.

The reservoir images, Figure 4a and 4b, also shows three wide roughly parallel low resistivity zones that connect the injector and producer. These zones are at the heel of each well, approximately at the center and toward the toe. At the heel of the wells, a 100 m wide zone is observed. This zone is associated with a known fracture corridor, recognized from production logs and recently mapped with image logs. This zone accepts more than 90% of injection water. This zone is cased in the producer, so there is no direct inter- well communication through

this fracture corridor. At the center of the two images, a second 100 m wide zone connecting the wells can be identified. This zone conforms to a large scale fracture zone identified from image logs. A third low resistivity zone can be found at the toe of the two horizontal wells.

Large sections of the inter-well volume are at the original resistivity values and appear to be unswept. These areas are identified as well targets for future new wells or sidetracks. A well is planned to be placed into one of these areas in 2015, partly justified on the basis of supplying further data for the EM R&D activities.

Conclusions

A crosswell EM survey, which was the first of its kind, has yielded good quality and very useful 3D images from a crosswell data set. The 3D inversion data have helped to identify swept and unswept volumes in a fractured waterflooded reservoir, which directly supports improved production and recovery efforts. This survey has illuminated the possibility of crosswell EM in nonvertical well geometries.

In the next phase of this project, a substantial effort will be made to reconcile logs, pressure, production and inter-well data into a consistent static and dynamic model. The outcome will be the most probable saturation distribution of fluids in the inter-well volume.

Acknowledgments

This project is the result of a collaborative multidisciplinary project between Saudi Aramco and Schlumberger. Special thanks to all the colleagues who made this success possible, among whom we mention: Danang Widjaja, Sanggam Hutabarat, Mark Ma, Keshab Baruah, Nashi Al-Otaibi, Moemen Ramadan, Steve Crary, Pablo Saldungaray, Khaled Hadj-Sassi and Joseph Khoury.

Reading this ad?

So are your customers!

Reach a wider customer base through our Signature Series magazines.

EPRASHEED
signature series

To advertise with EPRasheed Magazines contact sales@eprasheed.com

Water Problems?

It's easier if we all pull together.

Let us partner with you to control water break-through and optimize production.

We help you find the best remedial chemical combination using our Relative Permeability Modifier integrated program of High-tech independent laboratory testing and interpretation.

We also offer a wide range of laboratory services including High-tech Special Core Analysis; NMR Core Analysis and log interpretation; Formation Damage; Reservoir Characterization and PVT.

COREX

Your Partner For Success.

www.corex.co.uk

UK
Howe Moss Drive
Dyce, Aberdeen,
AB21 0GL
United Kingdom
Tel: +44 1224 770434
Fax: +44 1224 771716
E-Mail: sales@corex.co.uk

Egypt
176, Sector No.6,
Industrial Area
Zahraa El Maadi,
Helwan, Egypt
Tel: +202 25218446/7
Fax: +202 25175261
E-Mail: sales@corex.co.uk

Abu Dhabi
Corex AlMansoori
Corniche Road, Mussafah Base
Mussafah Industrial Estate
United Arab Emirates
Tel: +971 2 5559712/5554134
Fax : +971 2 5559713
E-Mail: sales@corex.co.uk

Reservoir Stress Path from 4D Coupled High Resolution Geomechanics Model: A Case Study for Jauf Formation, North Ghawar, Saudi Arabia

By Otto E. Meza Camargo, Dr. Tariq Mahmood and Dr. Ivan Deshenenkov.

Abstract

This study presents the full in situ stress tensor results, i.e., orientation and magnitude, for the Jauf formation at pre- and post-production conditions, and their use to build a 4D coupled one-way geomechanics model. These results were constrained by using existing data from wireline logs, downhole measurements and laboratory tests. After building 1D to 3D Mechanical Earth Models (MEMs) using data from 27 wells, the 3D model was used as input to the 4D coupled model for years A, B, C and D.

This study concluded that the Jauf formation in the study area is characterized by a strike-slip-faulting regime in which the maximum horizontal stress (S_{Hmax}) is the largest principal stress, i.e., S_{Hmax} > vertical stress (Sv) > minimum horizontal stress (S_{hmin}). The S_{Hmax} orientation, N75°E, was constrained by using borehole image logs.

The calibrated stress models were established based on poro-elastic equations, fracture closure pressures (FCPs), core data, wellbore stability models and drilling events depicting an average anisotropy ratio of approximately 1.2 to 1.4 (maximum principal stress magnitude)/(minimum principal stress magnitude). The stress model at pre-production conditions showed values for the pore pressure gradient of approximately ~0.62 psi/ft, for the S_{hmin} gradient of ~0.71 psi/ft to 0.95 psi/ft and for the S_{Hmax} gradient of ~1.3 psi/ft to 1.4 psi/ft.

The 3D geomechanics high resolution grid was created for elastic properties and rock strength parameters propagation; the latter was driven by the total porosity (PHIT) model as a controlling parameter. The range of the estimated values are:

- Young's modulus from 1.2 Mpsi to 6.0 Mpsi.
- Poisson's ratio from 0.24 to 0.38.
- Unconfined compressional strength (UCS) from 6.0 Kpsi to 16.0 Kpsi.

In the 4D coupled model, the FCP values from hydraulic fractures were used to calibrate the S_{Hmin} at post-production conditions over years A, B, C and D. The predicted stress model showed a good match with the FCP over the 27 wells used in this study. The reservoir stress path was defined over the grid model using the following:

$$\Delta S_{hmin} = 0.8055 * \Delta PP_{(Pore\_Pressure)} + 0.3762 \qquad (1)$$

The S_{hmin} stress average maps were generated from pre-

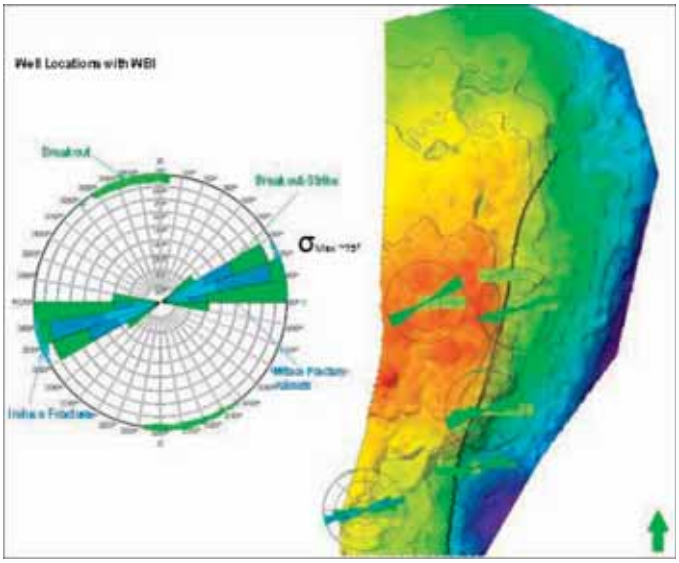

Fig. 1. S_{Hmax} direction in study area (N75 E ± 10) from borehole breakouts and drilling-induced fractures in the Jauf formation (Upper, Middle and Lower).

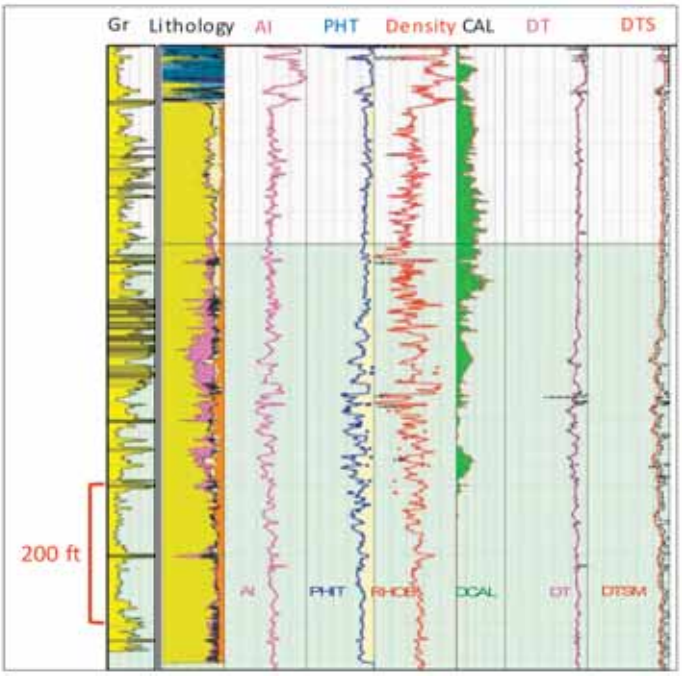

Fig. 2. Well log corrections were performed for sonic and density logs, using core information and multilinear regression equation analysis.

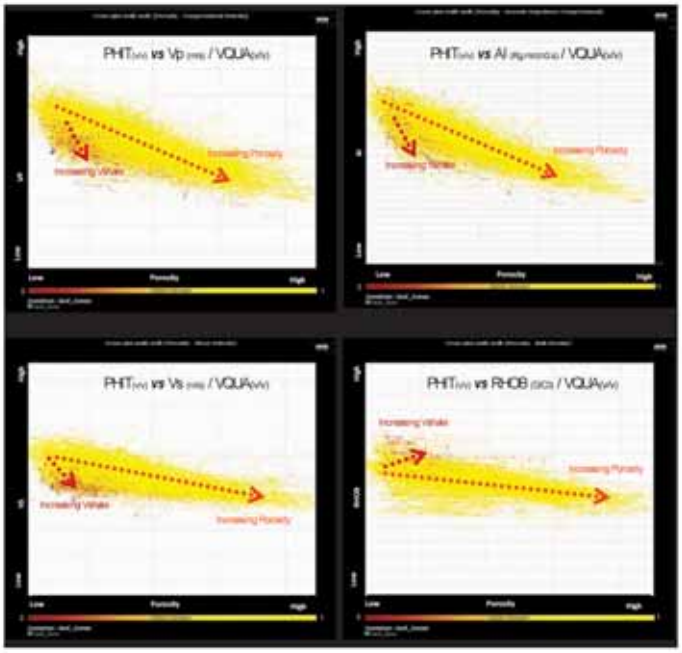

Fig. 3. Cross-plots were used to analyze the trends and relationship between different rock parameters with respect to the PHIT.

and post-production conditions in three stratigraphic levels (zones) of the Jauf formation – Upper, Middle and Lower. This study concluded that the Upper Jauf is relatively more stressed than the Middle Jauf and Lower Jauf. Breakdown pressure maps for these three stratigraphic levels were also generated and are presented in this study.

Introduction

The main objective of this study was to define the full in situ stress tensors at pre- and post-production conditions for the Jauf formation in the North Ghawar area and to build a 4D coupled one-way geomechanics model for the years A, B, C and D. 1D to 3D geomechanics models were built utilizing all available

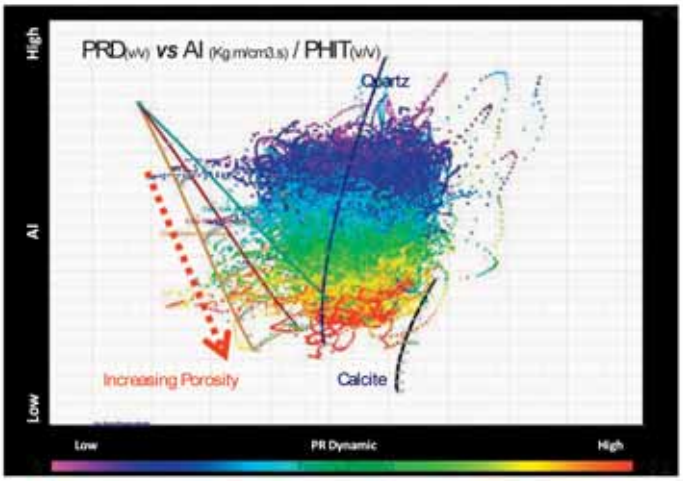

Fig. 4. Cross-plots between the Poisson's ratio and acoustic impedance showing the scatter of data over the Quartz zone.

data for 27 wells across the study area, and the 3D geomechanics model was used as a prerequisite input for the 4D coupled one-way geomechanics model.

The 4D calibrated model will be used to identify field-scale hydraulic fracturing "sweet spots" and to optimize hydraulic fracture design. In addition, the 4D geomechanics model will be used in well placement optimization and in the analysis of wellbore stability for horizontal wells.

The maximum horizontal stress (S_{Hmax}) direction, N75°E ±10°, was inferred from drilling-induced tensile fractures and borehole breakouts[1, 2] identified in the borehole image logs. Figure 1 shows the results of the stress direction analysis. No significant azimuthal rotation of the principal horizontal stress was identified across the study area.

Rock Physics Analysis

Well log corrections were performed for the sonic and density logs of all 27 wells using core information and multilinear regression equation analysis. Results from one of the wells are illustrated in Figs. 2 and 3.

Rock Physics Modeling

Rock physics models are mathematical equations based on physical principles that are used to generate P and S velocities based on rock structure, composition and properties. By setting some of the parameters, i.e., clay content, sand bulk and shear modulus, the equations can be solved to model velocities in missing data intervals. The main advantage of this approach is that all relations between elastic properties and rock quality are preserved.

The rock physics model is focused on predicting dynamic compressional velocity (Vp) and shear velocity (Vs) as accurately as possible, producing results suitable for further mechanical modeling. Using the porosity and clay content from well logs, an analysis was performed to determine which rock physics models are most suitable. The advanced differential effective medium modeling described by Prasad and Nur (2003)[3] was used to estimate P and S velocities. A tangential shear factor was introduced to obtain an optimal match with observed Vp/Vs ratios in the sandstones, since contact theory is known to overpredict shear wave velocities by neglecting rotational freedom and slip at grain contacts.

Vp and Vs are functions of porosity, clay content, differential pressure and saturation. The setup of the input parameters was completed iteratively to find the best solid clay properties for this dataset. This can be thought of as inverting for solid clay elasticity, assuming that all other properties are known and that our model is correct. Calculated Vp and Vs were then calibrated on dynamic mechanical properties derived from the core analysis to obtain the best fit between all available data, Figs. 4 and 5.

The dynamic rock properties obtained from ultrasonic core tests were used to calibrate the dynamic Poisson's ratio (PRD) and dynamic Young's modulus (YMD) for Well XX_A, Well XX_E and Well XX_C.

Pore Pressure and Minifrac Data

The pore pressure model at pre-production conditions was generated from direct measurements obtained through the modular formation dynamics tester and

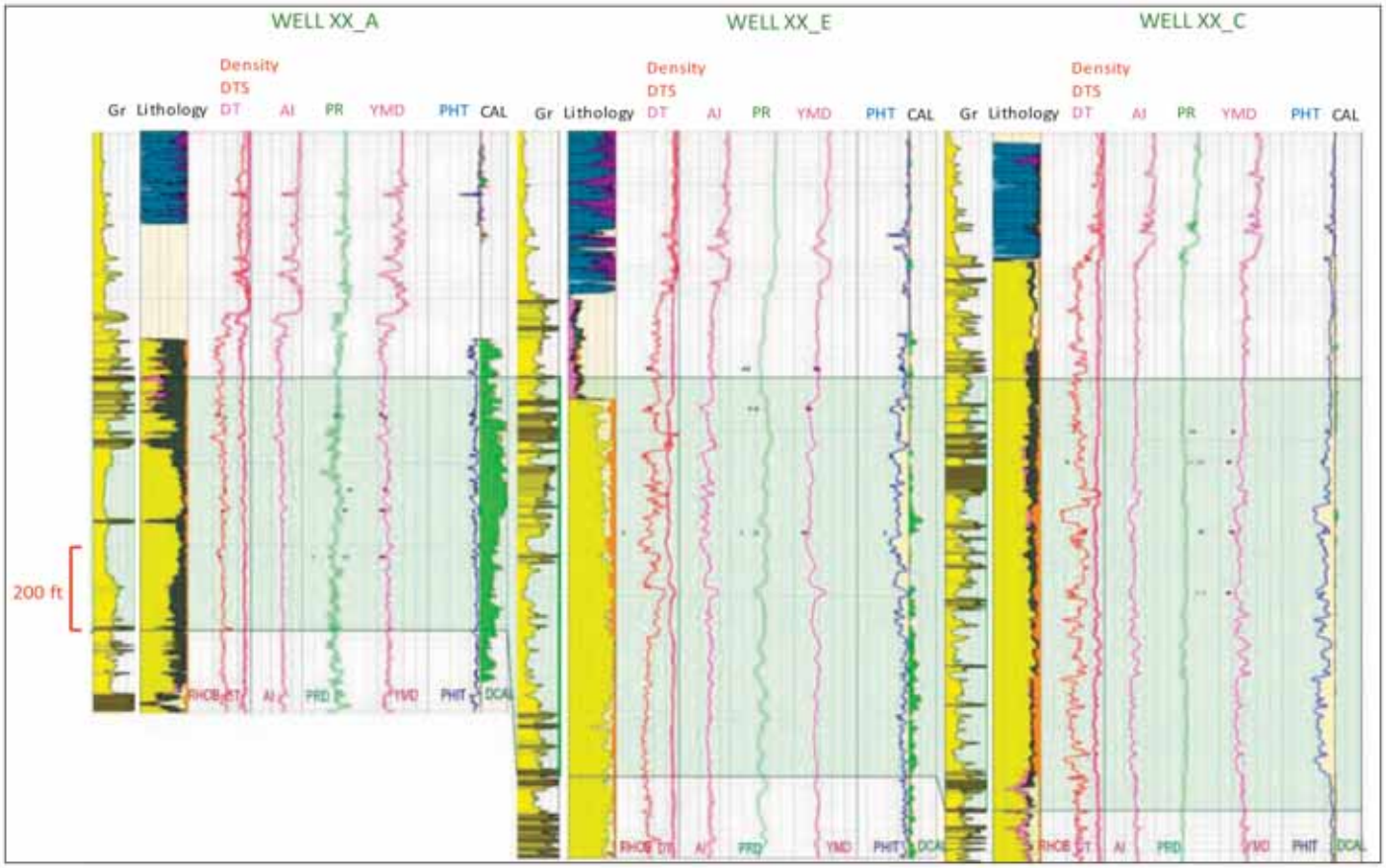

Fig. 5. Ultrasonic core test data was used to calibrate the dynamic rock properties derivate from sonic and density logs.

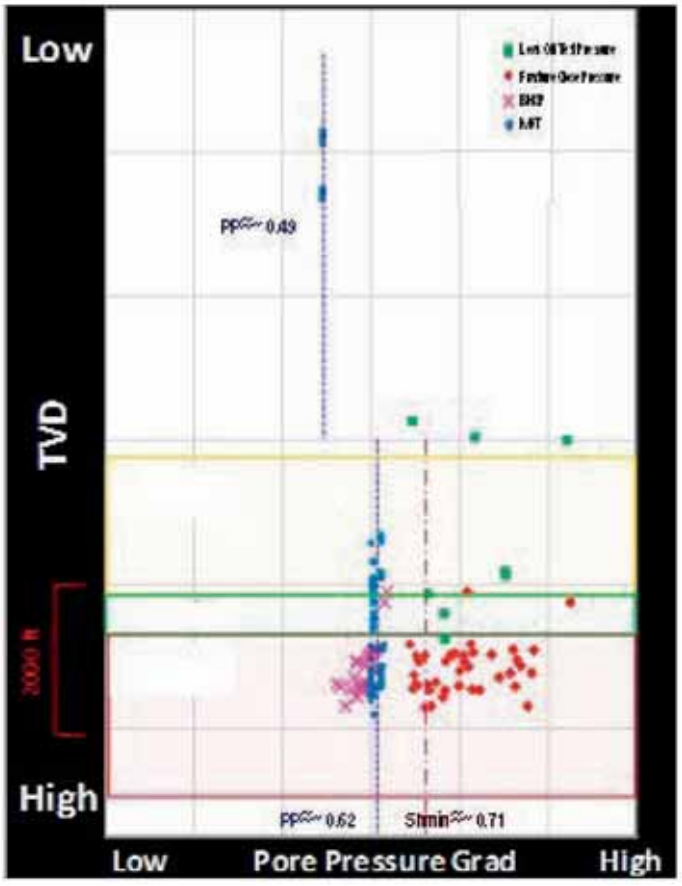

Fig. 6. FCP shows a wide dispersion effect (from 0.71 psi/ft to 0.98 psi/ft), which can be due to depletions.

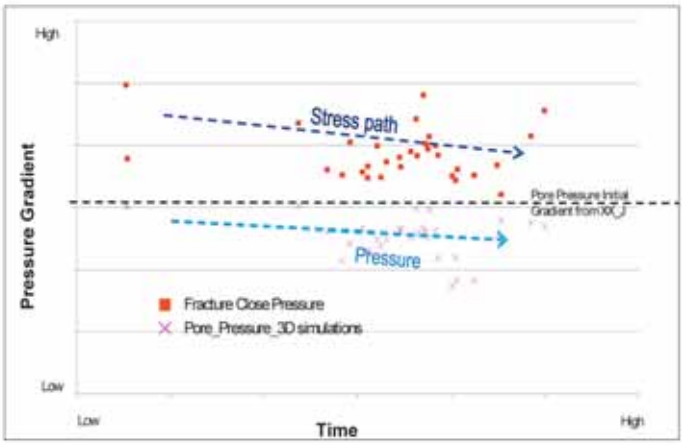

Fig 7. Pore pressure derived from 3D simulations and FCP plotted over time, show well-defined trends. The FCP-derived "stress path" is interpreted to result from depletions

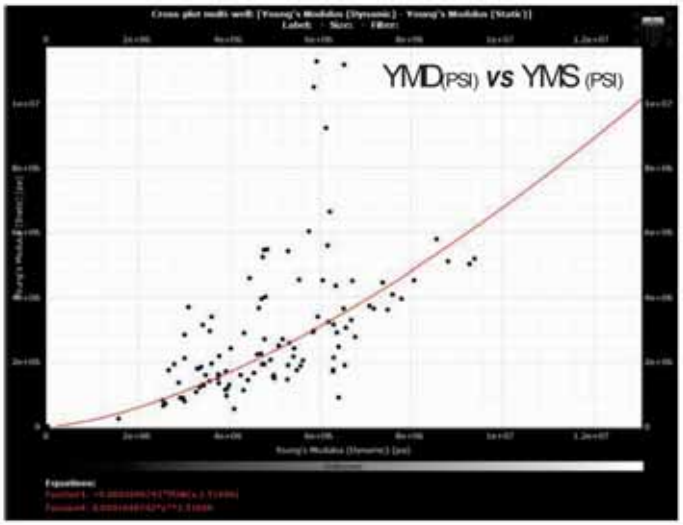

Fig 8. Tri-axial core, YMS and YMD relationship.

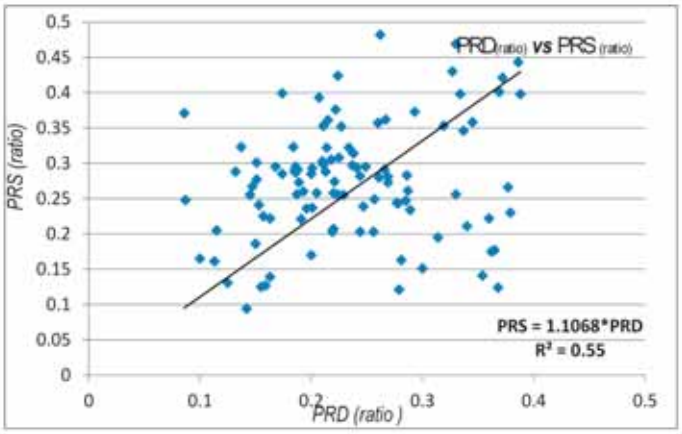

Fig 9. Static Poisson's ratio plotted with the PHIT, density and YMS. There are no direct relationships identified between the parameters.

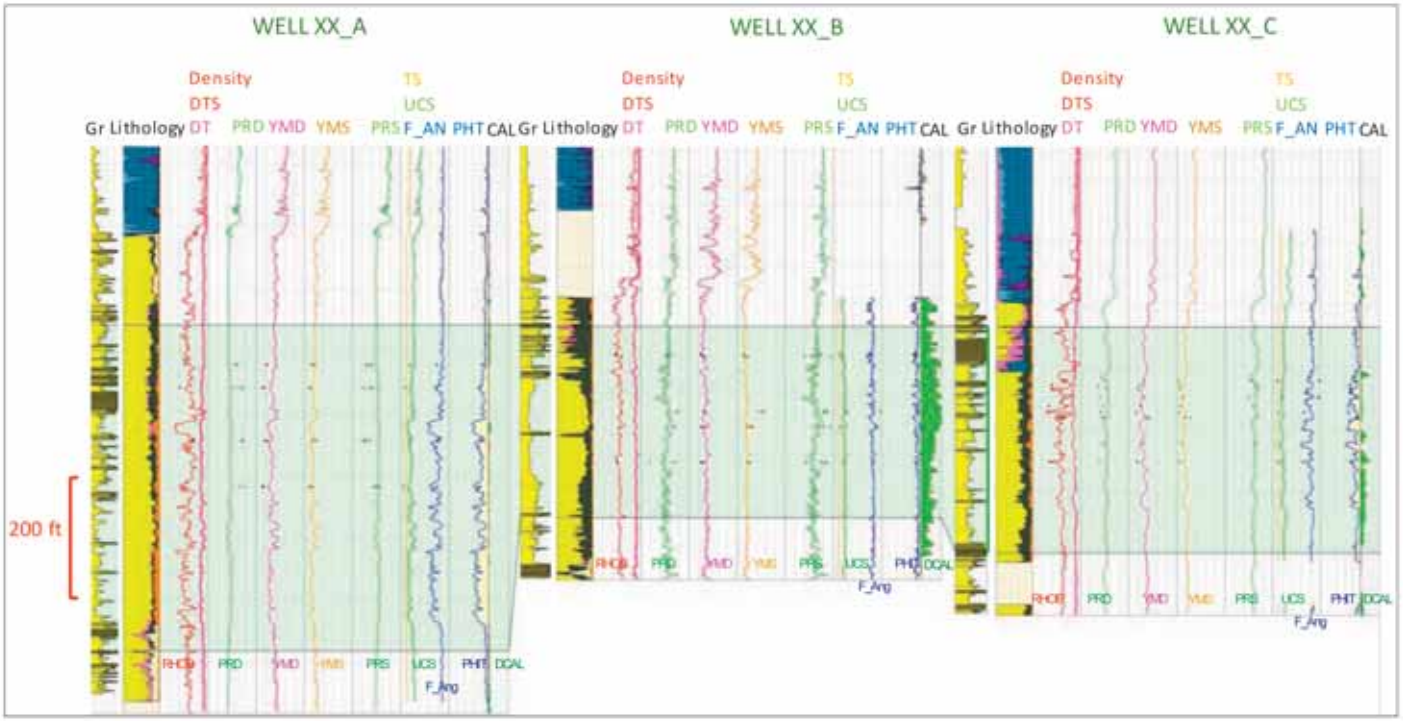

Fig 10. Well XX_W, Well XX_B and Well XX_C with static rock mechanics properties modeled using dynamic properties and core correlations.

from bottom-hole static pressure (BHSP) estimated from hydraulic fracturing in the Jauf formation, Fig. 6. Eaton's method was used for the pore pressure estimation, and the results were calibrated with the modular formation dynamics tester measurements, BHSP, mud weight (MW) and drilling events.

The BHSP estimated from hydraulic fracturing in the Jauf formation shows a wide variability, changing from 0.58 psi/ft to 0.62 psi/ft. This effect may be due to the depletions in the zones where the hydraulic fractures were performed.

The minimum stress values were estimated from the leakoff test and the fracture closure pressure (FCP). These also show a large variability across the study area, with values ranging from 0.71 psi/ft to 0.98 psi/ft. The initial pore pressure gradient in Well XX_J can be estimated as 0.62 psi/ft. The lower values are predicted because hydraulic fractures were performed over the depletion zones, which can reduce the FCP, Fig. 7.

Rock Mechanical Properties Correlations

Values for the YMD, shear modulus, bulk modulus and Poisson's ratio of the rock were generated from

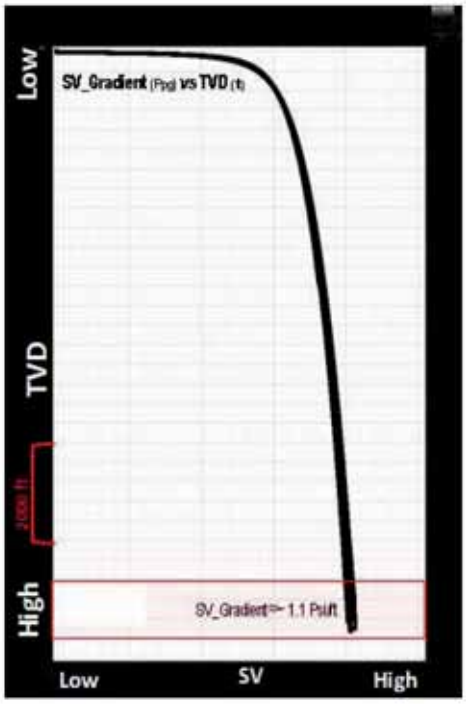

Fig. 11. Vertical stress was estimated from the density log..

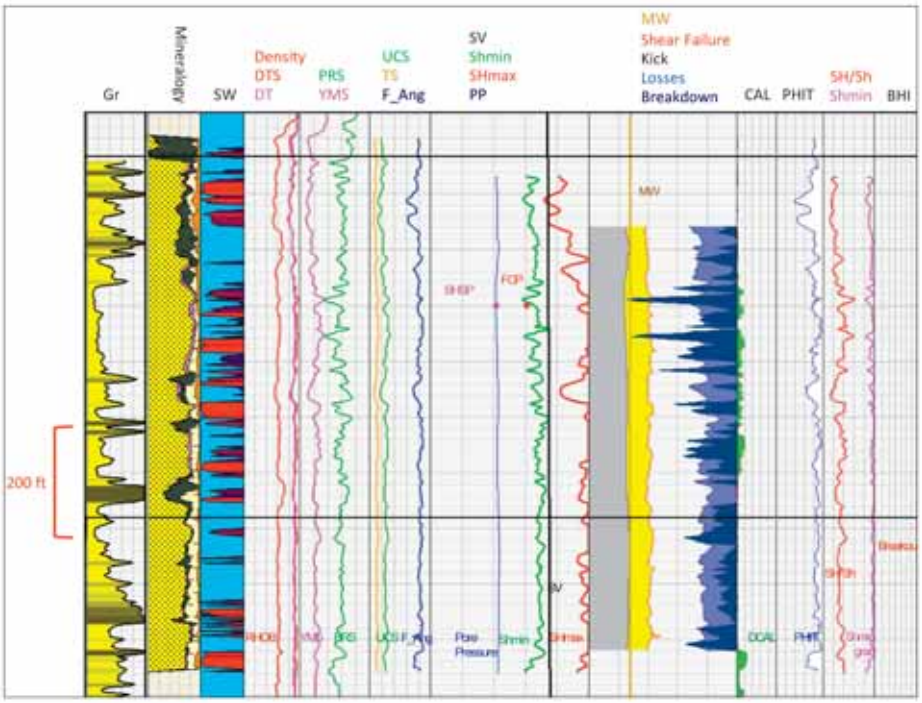

Fig. 12. Stress model and wellbore stability model for Well XX_D.

the compressional sonic, shear sonic and density logs. Converted static properties using empirical correlations from triaxial tests were also estimated. From these triaxial tests, a relationship was derived between the static Young's modulus (YMS) and YMD, Fig. 8. A derivative of the equation is:

$$YMS = 0.0001646742 * YMD^{1.51606} \quad (2)$$

The PRD was estimated with the poro-elastic equation, and the static Poisson's ratio was defined based on several correlations from the triaxial core tests using the porosity, bulk density, YMS and PRD results. No direct relationship was inferred between these properties, Figs. 9 and 10.

$$Static\_Poisson\_ratio = 1.15 * Dynamic\_Poisson\_Ratio \quad (3)$$

The unconfined compressional strength (UCS) was estimated using the multi-correlation between the YMS and total porosity (PHIT). The equations' result was:

$$UCS = 0.001405728*(YMS) - 19821.21*(PHIT) + 5828.503 \quad (4)$$

1D Mechanical Earth Model (MEM)

The Jauf formation is characterized by a strike-slip-faulting regime in which the S_{Hmax} is the largest principal stress — S_{Hmax} > vertical stress (Sv) > minimum horizontal stress (S_{hmin}). The orientation, N75°E, of the S_{Hmax} was inferred from borehole breakouts and drilling-induced tensile fractures interpreted from borehole images.

Vertical Stress

The overburden, or vertical stress, was evaluated using the density logs, which showed an average gradient of approximately ~1.1 psi/ft, Fig. 11.

Horizontal Stresses

The S_{hmin} and S_{Hmax} profiles were estimated using the poro-elastic and horizontal strain stress models, where the S_{hmin} and S_{Hmax} at each depth depended upon:

- Mechanical properties
- Pore pressure
- Vertical (overburden) stress

The S_{hmin} was also constrained by the FCP and leakoff test data[4]. The stress profiles were plotted together with MW windows.

The S_{hmin}, as estimated from the hydraulic fracture data, was found to lie in the range of approximately ~0.85 psi/ft to ~0.98 psi/ft.

The S_{Hmax} was estimated using the poro-elastic model, the wellbore stability model and drilling events. The wellbore stability model was also calibrated with the borehole image interpretation – identifying drilling-

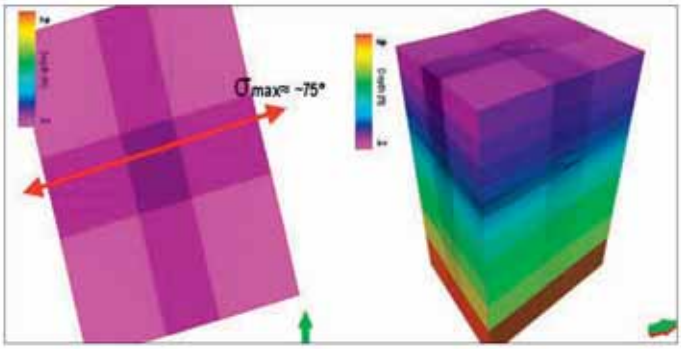

Fig. 13. Geomechanics grid orientation following the S_{Hmax} direction.

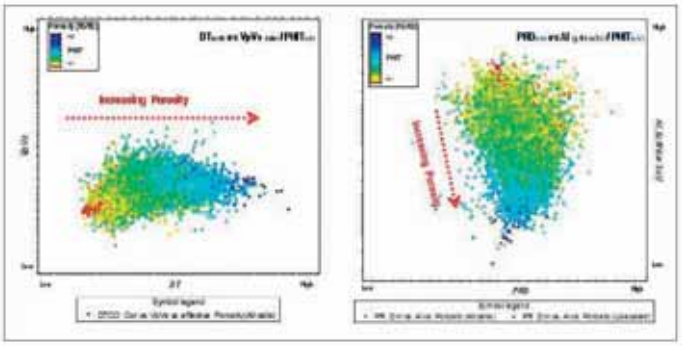

Fig. 14. Cross-plot over the 3D geomechanics grid properties extrapolations.

induced tensile fractures and breakouts. The estimated gradient of maximum principal horizontal stress magnitude is approximately ~1.3 psi/ft.

Stress Calibrations Using Drilling Events

Figure 12 shows the final wellbore stability calculation for Well XX_D. No major drilling issues were observed in the wells drilled through the Jauf formation except for Well XX_B (drilled in 2009), which reported a gas kick. The MW used to drill through this well was 9.8 pounds per gallon. There is good agreement between the calculated breakouts and the actual breakouts as interpreted from the borehole images[5].

Figure 12 also shows the main results from the 1D geomechanics process as follows:

- Track 1. Gamma ray.
- Track 2. Stratigraphy through the reservoir section.
- Track 3. Measured depth.
- Track 4. Mineralogical model estimated from petrophysics interpretation.
- Track 5. Water saturation estimated from petrophysics interpretation.
- Track 6. Density, compressional slowness and shear slowness.
- Track 7. Static rock properties – Poisson's ratio (light green) and Young's modulus (pink).

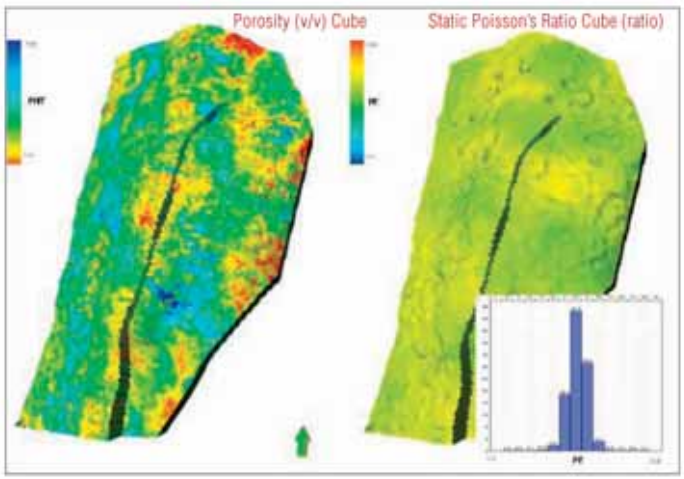

Fig. 15. Modeled 3D static Poisson's ratio.

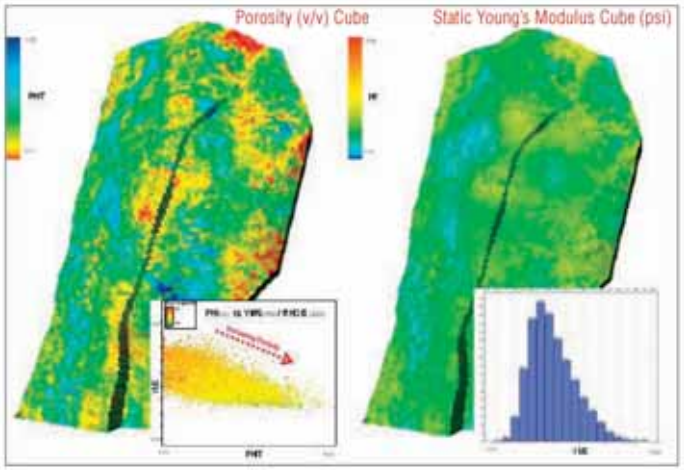

Fig. 16. Modeled 3D YMS.

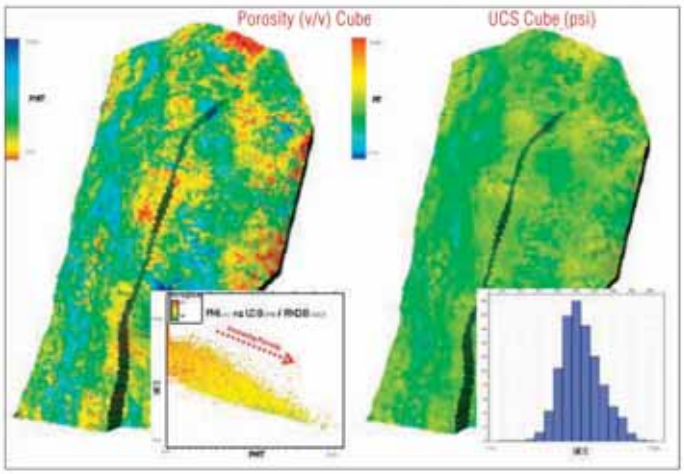

Fig. 17. Modeled 3D UCS.

Fig. 18. Boundary conditions used on the 3D MEM.

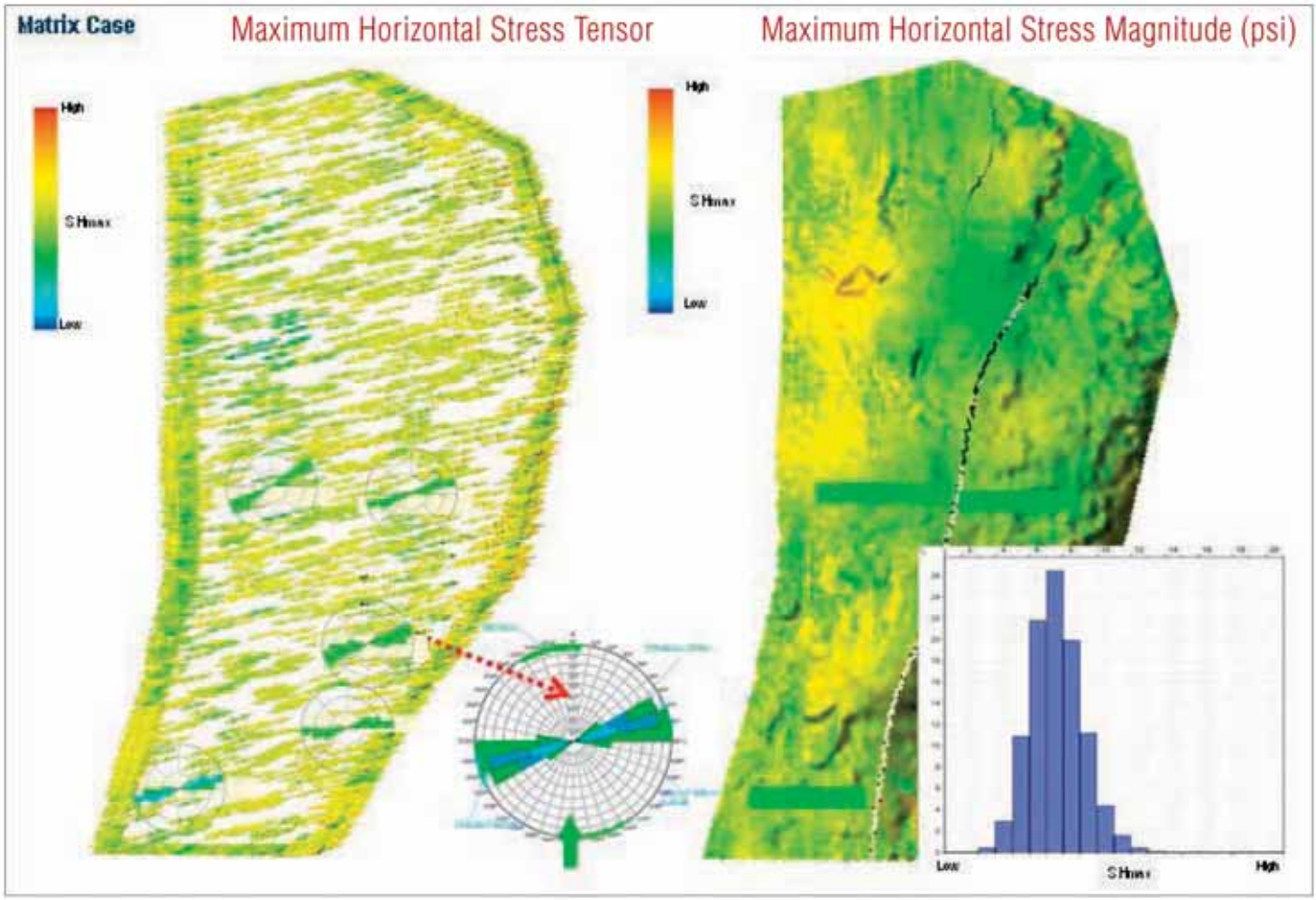

Fig. 19. SHmax tensor stress estimated from geomechanics simulations.

• Track 8. Rock strength properties – UCS (light green), friction angle (dark blue) and tensile strength (orange).
• Track 9. Calculated stress profiles – pore pressure (dark blue), S_{hmin} (green), S_{Hmax} (red), Sv (black), FCP (red dot) and BHSP (pink dot).
• Track 10. Calculation of the stable MW window; limits are calculated for kicks (gray), breakouts (red), mud losses (blue) and formation breakdown (purple), and the drilling MW (dark yellow line) is also shown.
• Track 11. Caliper logs.
• Track 12. PHIT.
• Track 13. Ratio between S_{Hmax}/S_{hmin} (red) and the S_{hmin} gradient (pink).
• Track 14. Breakout from borehole image interpretation (red).

3D Geomechanics Property Model

3D Grid Model

The geomechanics grid was oriented to follow the S_{Hmax} direction, N75°E, Fig. 13. The vertical and horizontal resolutions from the geomodel in the geomechanics grid were retained to capture the wide variability in the model. The geomechanics grid dimensions are:

• Total number of cells: 12 million.
• xinc = 100 m; yinc = 100 m; zinc ≈ 4.5 ft.

Propagations of Geomechanics Properties

The propagations of the properties were performed using the porosity model because it provided good correlation between Vp, Vs and density. A cokriging algorithm was used to extrapolate the well log data, which included Vp, Vs and bulk density, Fig. 14.

The 3D static rock properties were estimated based on the rock mechanics properties equations defined from the triaxial core test, with the range of the static Poisson's ratio being modeled from ~0.24 to ~0.38, Fig. 15.

The rock mechanics properties equations (Eqns. 2 and 3) were applied to estimate the YMS, Fig. 16, and the static Poisson's ratio based on the dynamic properties.

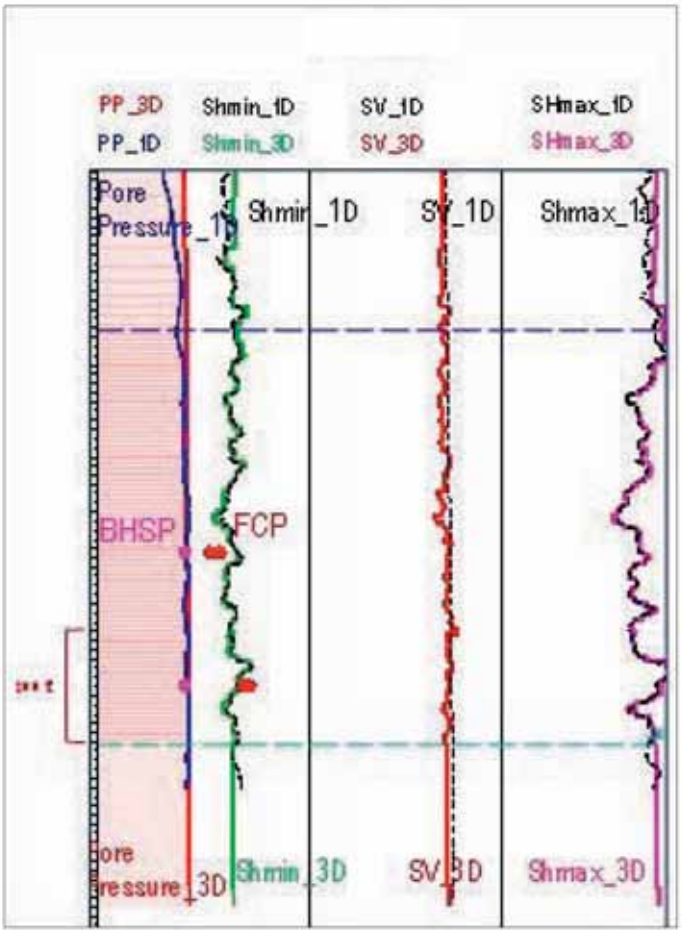

Fig. 20. Comparison between the 1D stress model (black) and the 3D stress model (S_{hmin} in green, Sv in red and S_{Hmax} in pink) for Well XX_J.

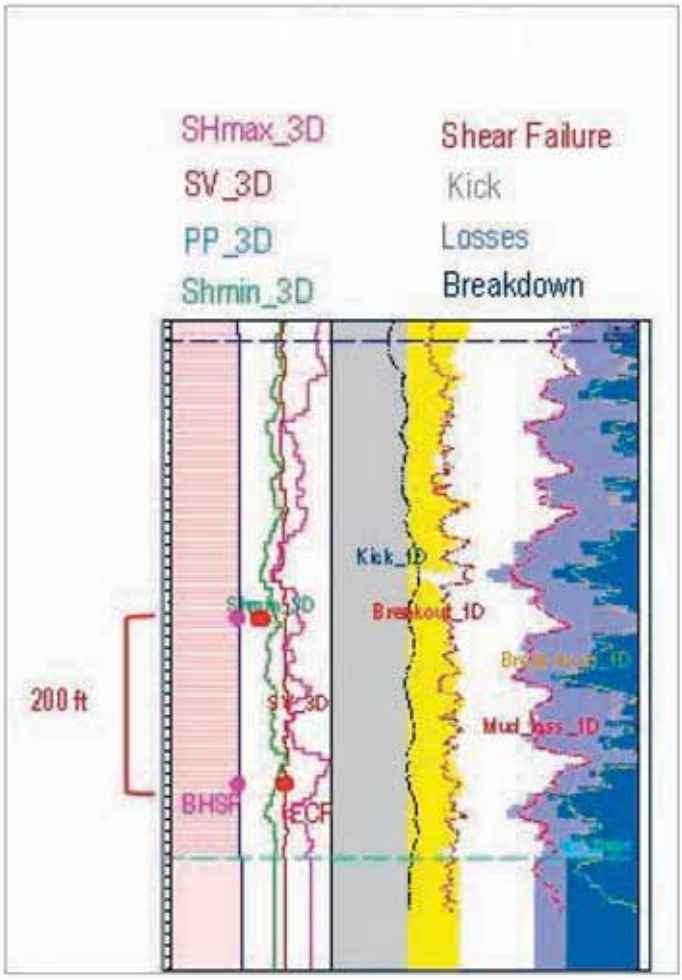

Fig. 21. Comparison between the 1D wellbore stability model (track 3 in dotted lines) and the 3D wellbore stability model (track 3 in filled colors) for Well XX_J.

The rock strength properties' UCS was estimated using Eqn. 4, Fig 17.

3D In Situ Stress Model

3D Stress Estimations

The first stage of a 3D stress analysis involves calculating stresses that represent the pre-production conditions throughout the reservoir and its surroundings. Due to the complex variations in structure and properties within the model, the stress equilibrium must be solved numerically. A finite element method was used to determine the required solution, producing a 3D map of stress magnitudes and orientations that vary both laterally and vertically. The model then uses the structure and rock mechanical properties defined in the preceding sections, together with the loads that govern stresses – gravitational, pore pressures and boundary conditions – to simulate the initial stress state of the field.

The results are calibrated to in situ stress profiles from the 1D MEMs. To address a number of uncertainties in the input data, such as the assigning of fault stiffness and the propagation of mechanical properties, a number of simulations were performed to assess the sensitivity to those parameters, Fig. 18.

Stress Initializations

The model was initialized on year A as describing pre-production conditions based on two cases: Matrix and Matrix + Faults. Both models considered the same boundary conditions, and the maximum, minimum and vertical stresses were computed as tensor stress, Fig. 19.

Comparisons between the 1D and 3D Stress Models

When comparing the stresses between the 1D and 3D MEMs, it is not expected that all three principal stresses of the 3D MEMs will match those of the 1D MEMs

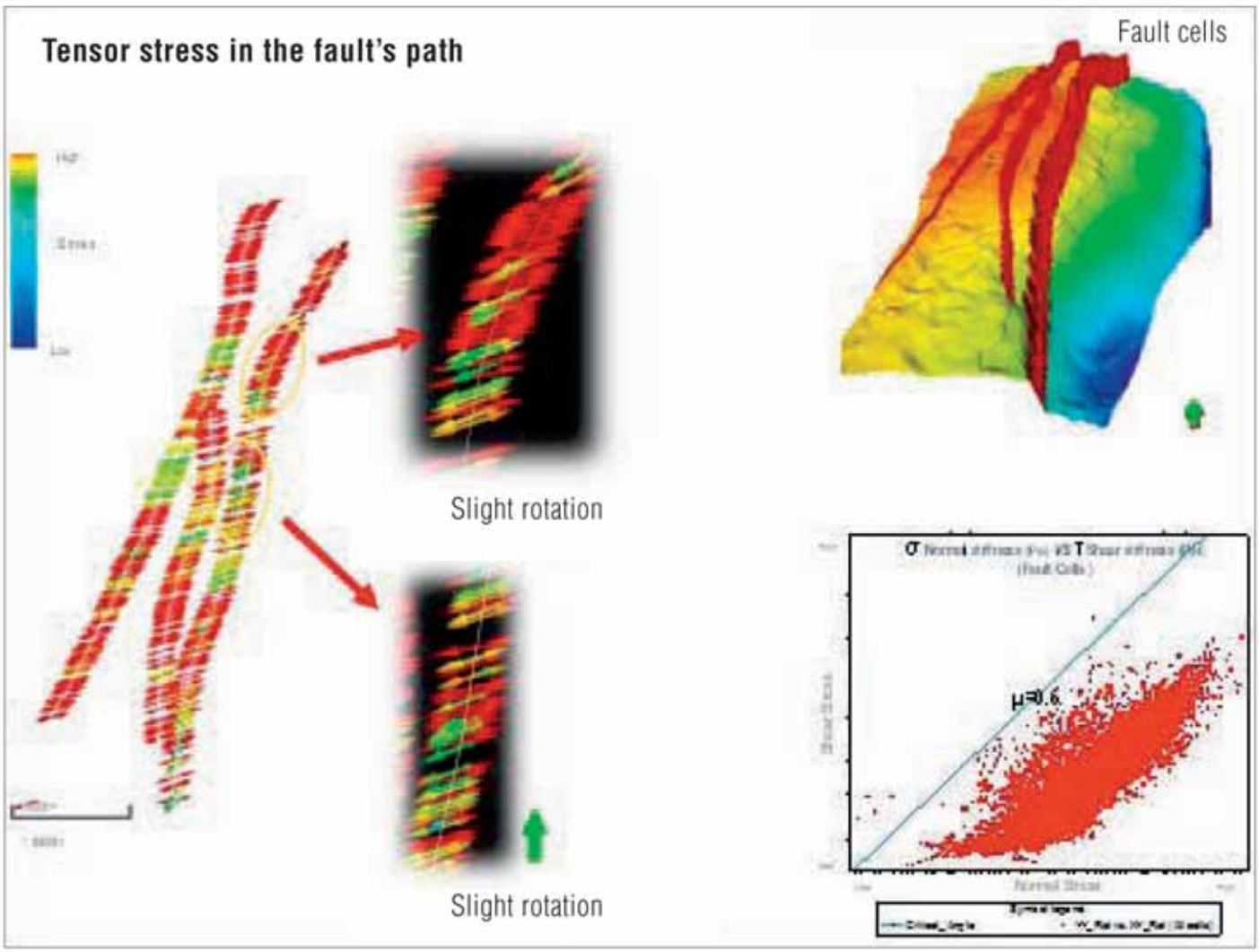

Fig. 22. Fault simulations case, showing the normal and shear stress for cells within faults.

exactly. One of the advantages of the 3D model is that it accounts for interactions that the 1D approach is unable to, for example:

- Vertical stress being different from the 1D integration of overburden weight.
- Magnitude and orientation changes of stress due to nearby faults.
- Consistent stress and strain variation between strong and weak layers.

The goal is therefore to ensure that the general magnitude and trend of the stresses is honored, while also expecting differences in the details. The comparison is valuable, however, because it provides a way of checking that the overall calibration of the 3D model is correct, particularly regarding the choice of boundary conditions.

In general, the match between the stresses obtained from the 1D MEM (stress model) and the 3D MEM (stress model) is good at initial conditions, Fig. 20. In

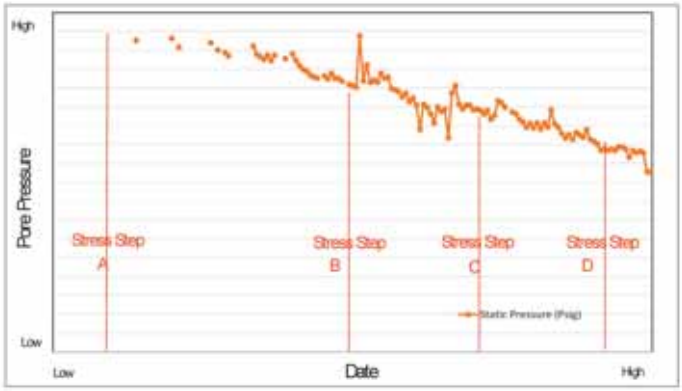

Fig. 23. Pore pressure and stress steps defined for years A, B, C and D.

the Matrix case, the relatively good match was achieved in 11 wells in the Jauf formation.

Comparison of 1D and 3D Wellbore Stability Models

The 3D wellbore stability model was estimated using the 3D geomechanics model and compared with the 1D wellbore stability results. In both cases, the match

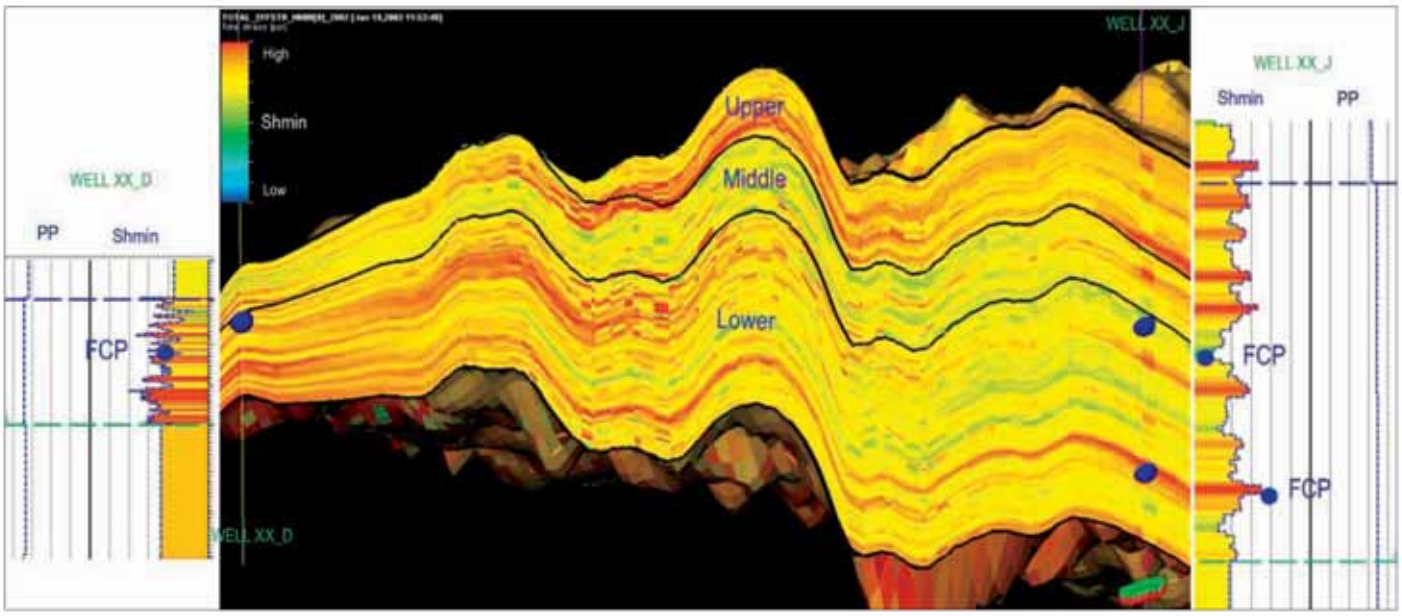

Fig. 24. 3D cross-section showing the S_{hmin} initialization, compared with the FCP (hydraulic fracture over year A) for year A.

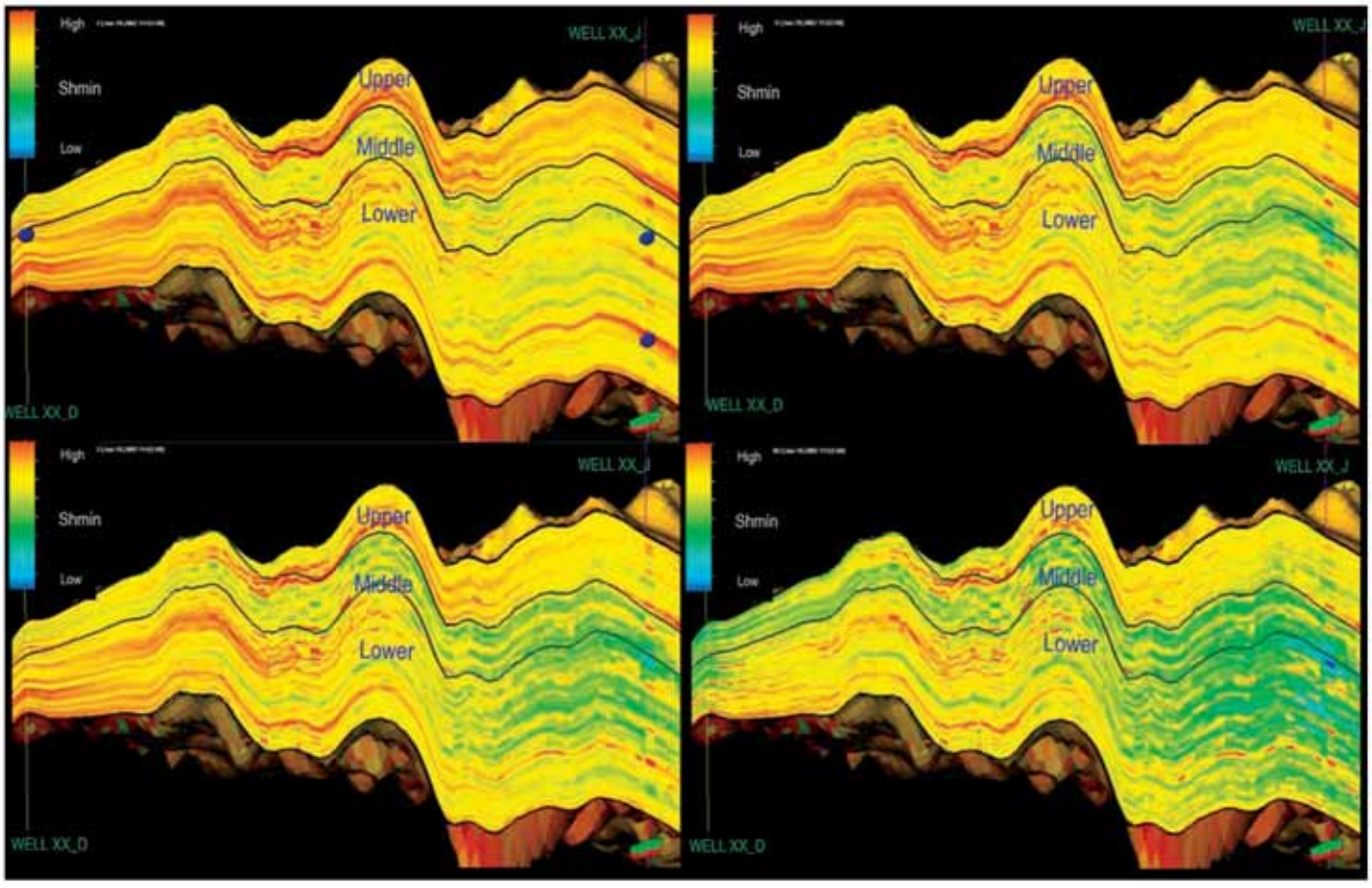

Fig. 25. 3D cross-section through Wells XX_D to XX_J, showing the S_{hmin} at pre-production conditions and over time.

was consistent under the boundary conditions defined for the 3D geomechanics simulations model. Some of the wells were considered depleted in the 1D MEM (wellbore stability model) for calibration proposes. The estimated kick (pore pressure gradient), shear failure (breakouts), mud loss and breakdown pressure all showed a good match, Fig. 21, Track 3.

Faults Stability Analysis

To evaluate the fault stability[6] at pre-production conditions, the normal stiffness and shear stiffness were estimated – under the same boundary conditions – using the following geomechanics fault properties:

- Fault normal stiffness: 7.67E+06 KPa/m.

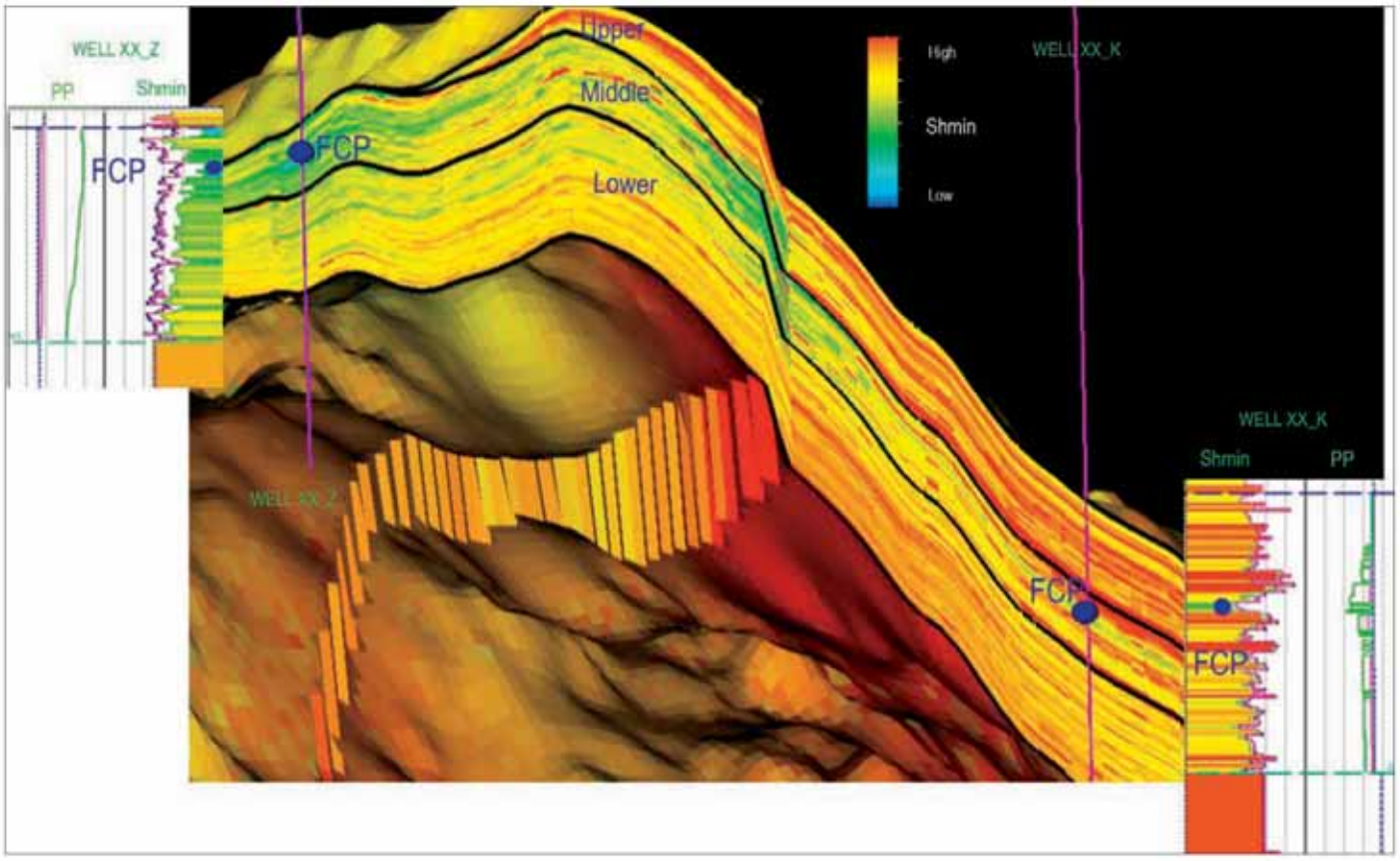

Fig. 26. 3D cross-section showing the S_{hmin}, compared with the FCP (hydraulic fracture year D) for year D.

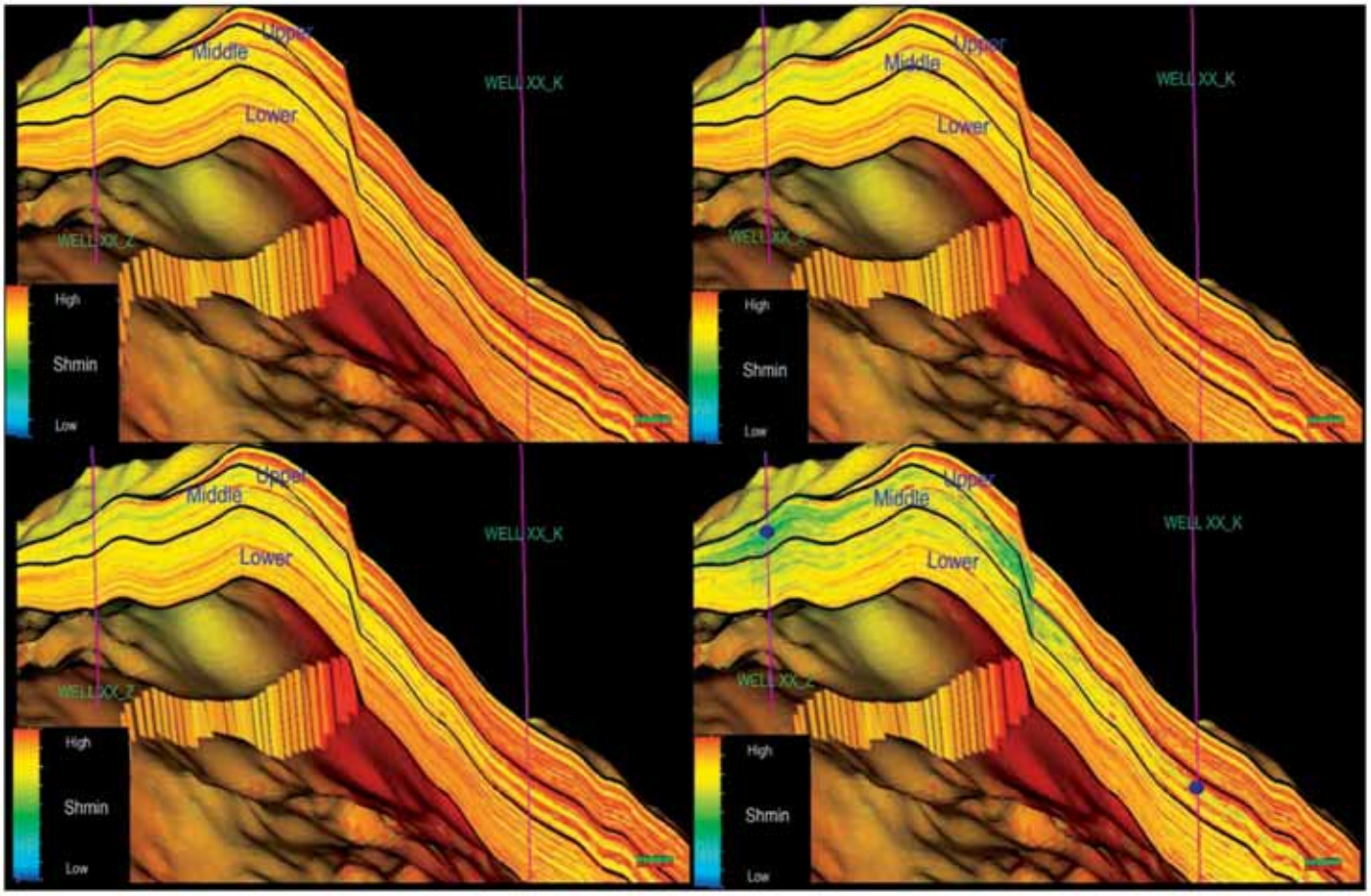

Fig. 27. 3D cross-section showing the S_{hmin} through Well XX_Z and Well XX_K at pre-production conditions and over time.

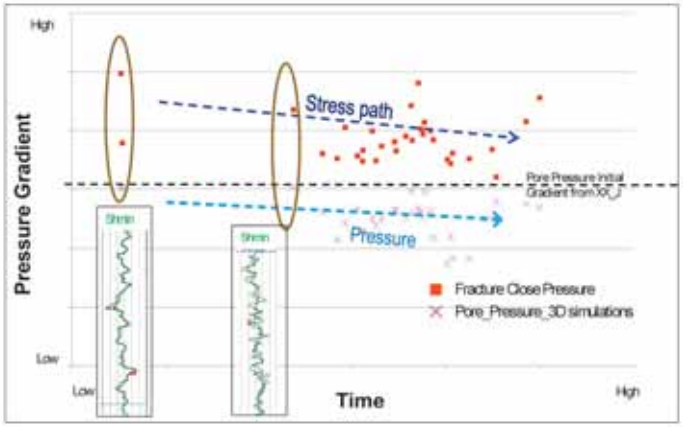

Fig. 28. The pore pressure from 3D simulation results and FCP plotted over time, showing the possible trend for the reservoir stress path.

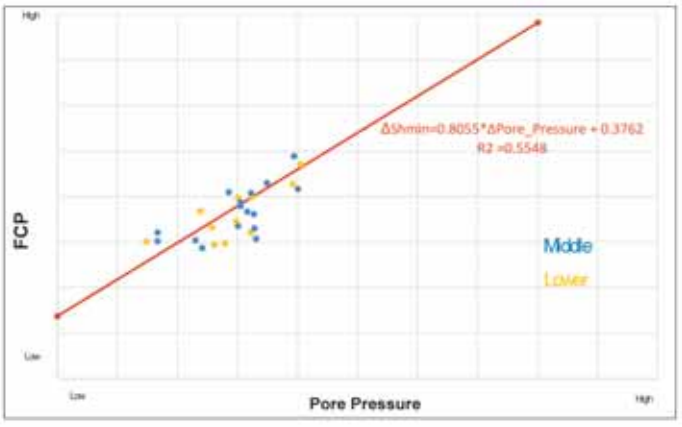

Fig. 29. Reservoir stress path defined by the relationship between S_{hmin}/Pp and FCP through to the reservoir depletions.

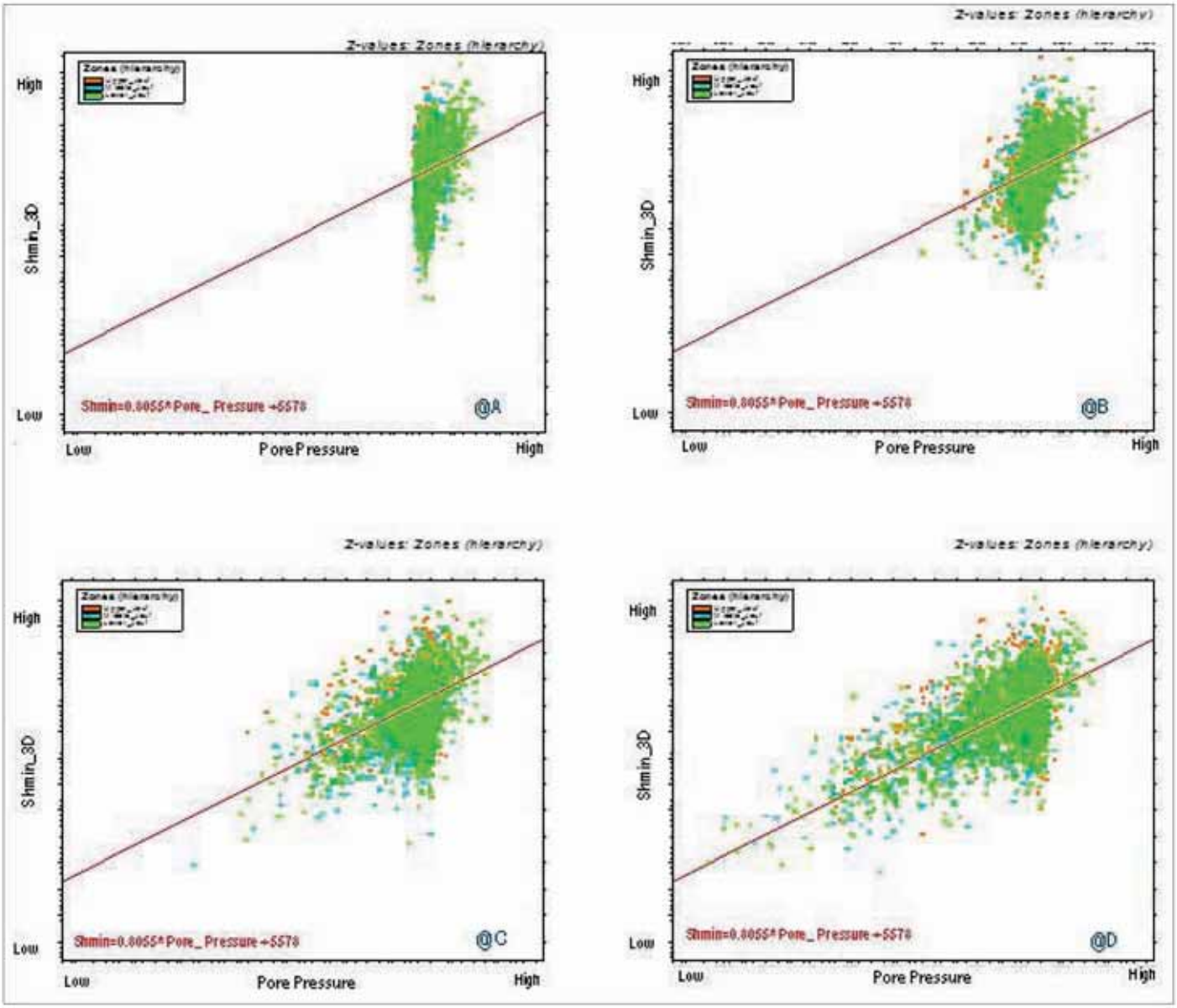

Fig. 30. Reservoir stress path defined by the relation between Pp 3D and S_{hmin} 3D from simulations, over depletions time.

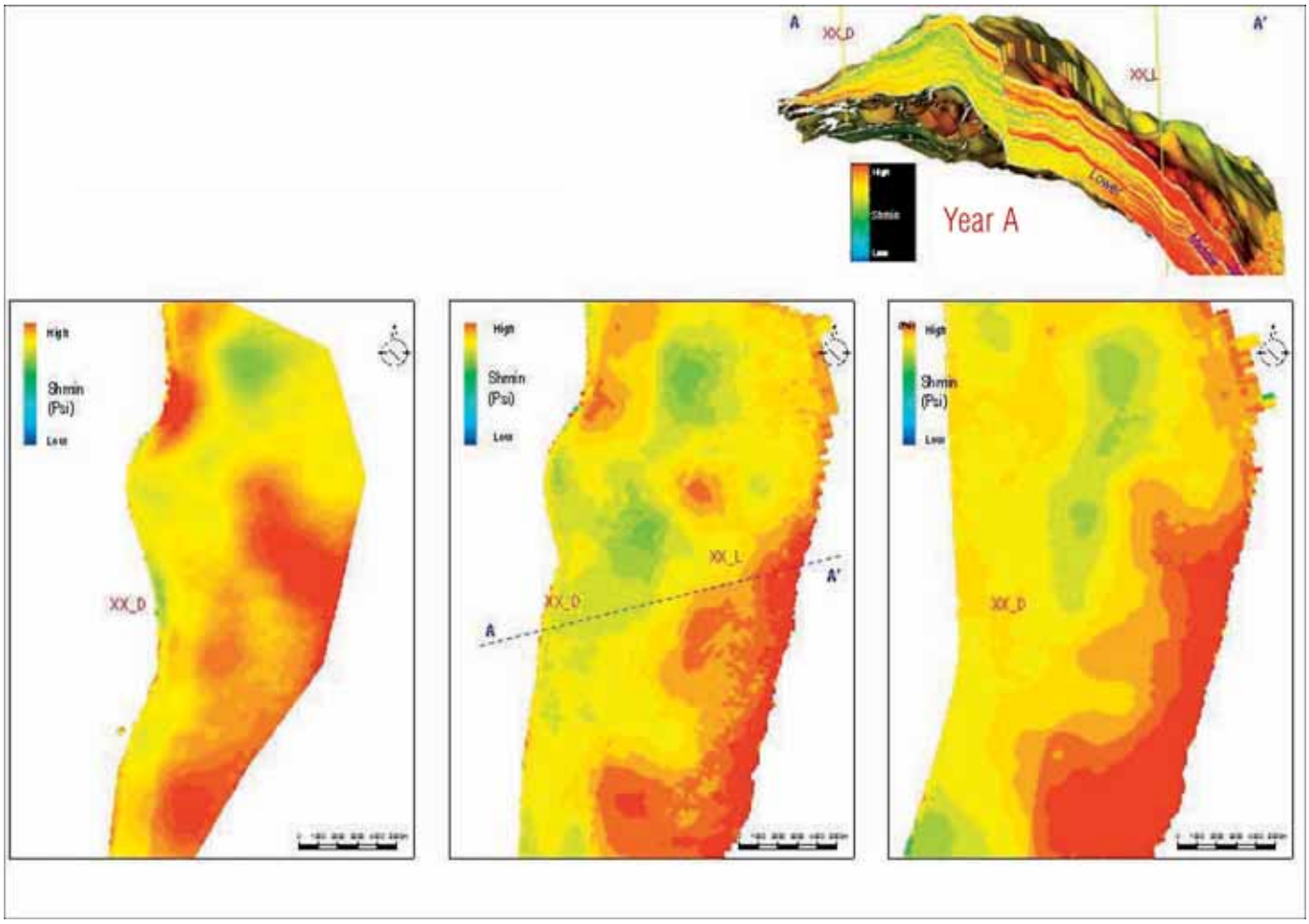

Fig. 31. Year A S_{hmin} average stress map for the Upper (left), Middle (middle) and Lower Jauf (right).

- Fault shear stiffness: 2.35E+06 KPa/m.
- Friction angle: 20°.
- Cohesion: 1 Kpa.

From the borehole image interpretations, no signifiant rotation of stress-induced[5] features – drilling-induced tensile fractures and breakouts – was observed along depth, suggesting either that the influence of faults and fractures was minimal or that there are no minor faults in the vicinity of these wells. Although some slight rotations can be identified in the tensor stress model for the faults, these are still inside the S_{Hmax} range. The normal stress and shear stress were computed for each cell in the faults showing stable conditions, Fig. 22.

4D Coupled One-Way Geomechanics Model

Stress Step and Pore Pressure Changes

The stress step calibrations were selected from the pore pressure profile to simulate the stress conditions over years A, B, C and D, Fig. 23.

Stress Variations over Time

The stress calibration from pre- to post-production conditions was performed taking the FCP measured from the wells over time[7]. In Figs. 24 and 25, the FCPs from Well XX_D and Well XX_J were compared with the 3D S_{hmin} simulation for initial conditions (year A), reaching a good match.

In year D, the FCPs from Well XX_Z and Well XX_K were compared with the 3D S_{hmin}, showing a good match, Figs. 26 and 27.

Reservoir Stress Path

In normal depletion behavior, the effective vertical stress increases at the same rate that pore pressure decreases because the total vertical stress is unaffected by changes in pore pressure. Subsequently, the effective horizontal stress increases more slowly during depletion than the pore pressure decreases. The total horizontal stress decreases with pore pressure following the S_{hmin}/ pore pressure coupling ratio[8-10], Fig. 28.

Figure 29 shows the relationship defined between the S_{hmin}/ pore pressure ratio with a value of 0.805 and the FCP, which can be considered as a normal range for a

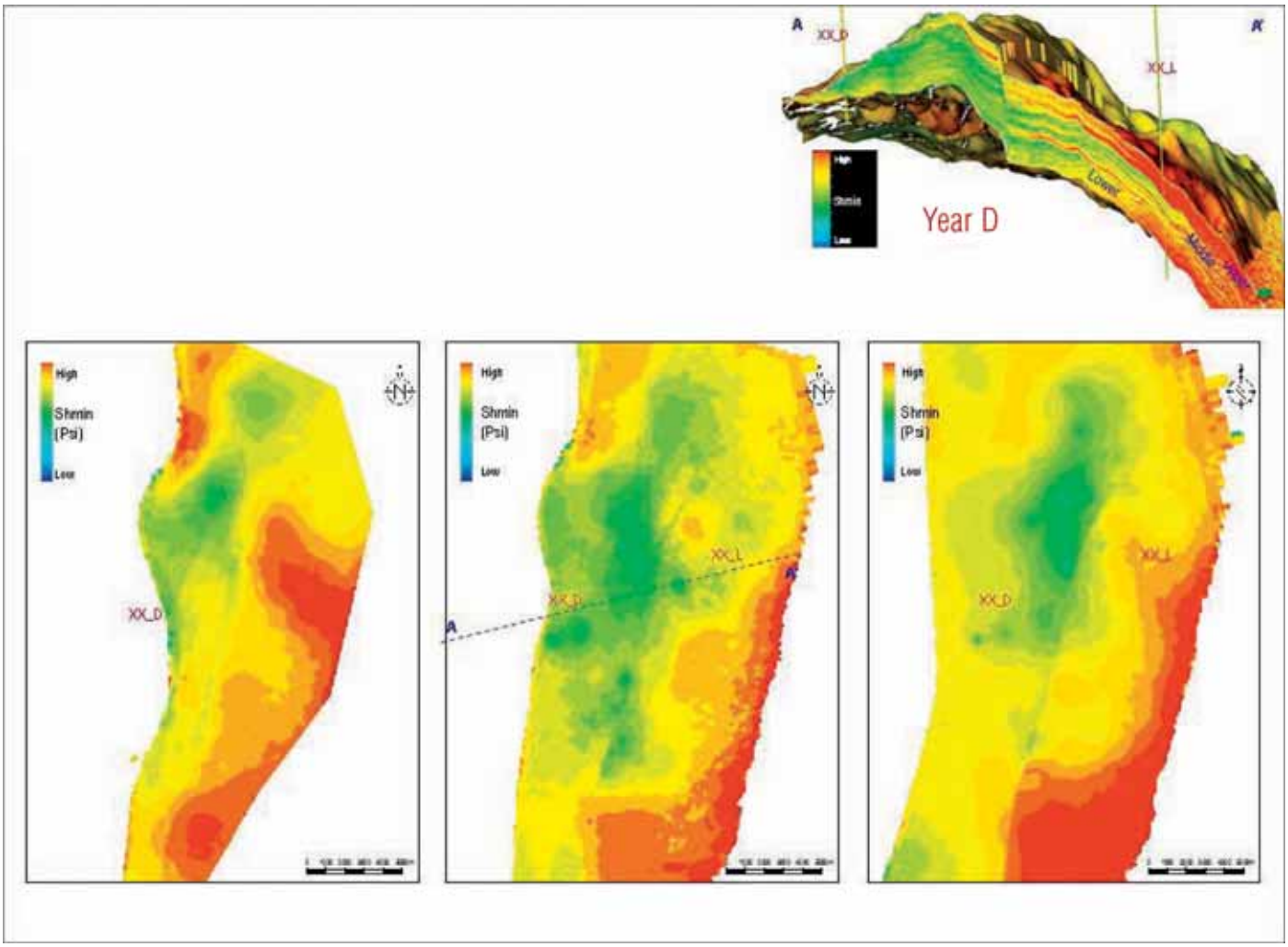

Fig. 32. Year D S_{hmin} average stress map for the Upper (left), Middle (middle) and Lower Jauf (right).

strike-slip-faulting regime. It was assumed that the drop in S_{hmin} with the pore pressure is nonrecoverable and that the S_{hmax} does not increase with a re-pressurization process.

In the 4D coupled one-way geomechanics model, the stresses obtained for the three stratigraphy levels defined for the Jauf formation – Upper, Middle and Lower – show almost the same behavior regarding the pore pressure and S_{hmin} relationship. This can be deduced from Fig. 30, where the Middle and the Lower Jauf are overlapping.

During the depletion process over years A, B, C and D, the pore pressure and S_{hmin} follow the stress path previously defined in Fig. 29, reaching in year D depleted zones where the pore pressure values are less than the original pressures. Following the stress path defined at post-production conditions, separate trends were identified for the Upper, Middle and Lower Jauf.

Stress Maps

S_{hmin} stress average maps were generated for each stress step and the three levels defined for the Jauf formation, showing important changes throughout the formation.

For the pre-production conditions (year A), Fig. 31, the S_{hmin} stress average map shows:

- In the Upper Jauf section, high stress values from the southwest area, e.g., Well XX_L, and lower values from the central part of the reservoir, e.g., Well XX_D.
- In the Middle Jauf section, lower stress in comparison with the Upper Jauf section, but still with high stress in the southwest area – Well XX_L.
- In the Lower Jauf section, high stress in the southwest area but less stress in the central area, e.g., Well XX_D.

The post-production conditions for years B, C and D show important reductions in the stress due to depletions in the Middle Jauf. The stress map over the Lower Jauf also shows significant reductions in

the central part of the reservoir near Well XX_D. The southwest part keeps the high stress values for the Upper, Middle and Lower Jauf around Well XX_L, Fig. 32.

Conclusions

The Jauf formation in the study area is characterized by a strike-slip-faulting regime in which the S_{Hmax} is the largest principal stress, i.e., $S_{Hmax} > Sv > S_{hmin}$. The S_{Hmax} orientation, N75°E, was constrained by using borehole image logs.

The calibrated stress models were established based on poro-elastic equations, FCP, core data, wellbore stability models and drilling events showing an average anisotropy ratio of approximately 1.2 to 1.4 (maximum principal stress magnitude)/ (minimum principal stress magnitude). The stress model at pre-production conditions showed values in the pore pressure gradient of ~0.62 psi/ft, the S_{hmin} gradient of ~0.71 psi/ft to 0.95 psi/ft, and the S_{Hmax} of around ~1.3 psi/ft to 1.4 psi/ft.

The high resolution 3D geomechanics grid was used to propagate the elastic properties and rock strength using the PHIT model as the main drive; the ranges of estimated values were as follows: Young's modulus from 1.2 Mpsi to 6.0 Mpsi, Poisson's ratio from 0.24 to 0.38, and UCS primarily from 6.0 Kpsi to 16.0 Kpsi.

In the 4D coupled model, the FCP values from the hydraulic fractures were used to calibrate the S_{hmin} at post-production conditions over years B, C and D. The predicted stress model gave a good match with the FCP over the 27 wells where data was available, with the reservoir stress path defined over the grid model by the following equation:

$$\Delta S_{hmin} = 0.8055 * \Delta PP_{(Pore\_Pressure)} + 0.3762 \quad (5)$$

The S_{hmin} stress average maps were generated from pre- to post-production conditions for the three stratigraphy levels – Upper, Middle and Lower Jauf – showing more stress in the Upper Jauf in comparison with the Lower and Middle Jauf sections. The southwest area shows the highest stress values of the three levels, > ~13,000 psi, even at post-production conditions.

Acknowledgments

The authors would like to thank the management of Saudi Aramco for their support and permission to publish this article. The authors would also like to thank Khaqan Khan, Jubril Oluwa and Thamer A. Sulaimani for their contributions to this project.

References

1. Bell, J.S.: "Practical Methods for Estimating In Situ Stresses for Borehole Stability Applications in Sedimentary Basins," Journal of Petroleum Science and Engineering, Vol. 38, Nos. 3-4, June 2003, pp. 111-119.

2. Prensky, S.: "Borehole Breakouts and In Situ Rock Stress – A Review," The Log Analyst, Vol. 33, No. 3, 1992, pp. 304-312.

3. Prasad, M. and Nur, A.: "Velocity and Attenuation Anisotropy in Reservoir Rocks," SEG paper 2003-1652, presented at the Society of Exploration Geophysicists International Exposition and Annual Meeting, Dallas, Texas, October 26-31, 2003.

4. Raaen, A.M., Skomedal, E., Kjørholt, H., Markestad, P. and Økland, D.: "Stress Determination from Hydraulic Fracturing Tests: The System Stiffness Approach," International Journal of Rock Mechanics and Mining Sciences, Vol. 38, No. 4, June 2001, pp. 529-541.

5. Kirsch, E.G.: Die Theorie der Elastizität und die Bedürfnisse der Festigkeitslehre, Springer, Dresden, Germany, 1898, 11 p.

6. Zoback, M.D.: Reservoir Geomechanics, Cambridge University Press, Cambridge, U.K., 2010, 461 p.

7. Koutsabeloulis, N.C., Heffer, K.J. and Wong, S.: "Numerical Geomechanics in Reservoir Engineering," in H.J. Siriwardane and M.M. Zaman (eds.), Computer Methods and Advances in Geomechanics, A.A. Balkema, Rotterdam, The Netherlands, 1994.

8. Santarelli, F.J., Tronvoll, J.T., Svennekjaier, M., Skeie, H., Henriksen, R. and Bratli, R.K.: "Reservoir Stress Path: The Depletion and Rebound," SPE paper 47350, presented at the SPE/ISRM Rock Mechanics in Petroleum Engineering, Trondheim, Norway, July 8-10, 1998.

9. Hillis, R.R.: "Coupled Changes in Pore Pressure and Stress in Oil Fields and Sedimentary Basins," Petroleum Geoscience, Vol. 7, No. 4, December 2001, pp. 419-425.

10. Breckels, I.M. and van Eekelen, H.A.M.: "Relationship between Horizontal Stress and Depth in Sedimentary Basins," Journal of Petroleum Technology, Vol. 34, No. 9, September 1982, pp. 2191-2199.

Biographies

Otto E. Meza Carmargo joined Saudi Aramco in 2014 as a Geologist Engineer working in the Exploration Technical Services Department. He has 10 years of experience in the oil industry, and prior to joining Saudi Aramco, he worked in a variety of geological positions across the Middle East region, Brazil, Peru and the U.K. Otto's experience includes several aspects of reservoir characterization and integrated geomechanics modeling for conventional and unconventional reservoirs.

He received his B.S. degree in Geological Engineering from the University of San Marcos, Lima, Peru..

Dr. Tariq Mahmood joined Saudi Aramco in 2008 and is currently working as a Geological Specialist/ Geomechanics Team Leader in the Exploration Technical Services Department. He began his career in 1996 working in Perth, Australia, for Z&S Geoscience/Baker Hughes, specializing in fractures/ faults characterization from borehole images. Tariq has provided consultancies to the major oil companies in the Asia Pacific region and Australia, including Shell Brunei, Petronas, Chevron, Santos, Apache, Woodside, etc.

He is a member of the American Association of Petroleum Geologists (AAPG), the European Association of Geoscientists and Engineers (EAGE) and the Dhahran Geosciences Society (DGS).

In 1996, Tariq received his Ph.D. degree in Structural Geology from the University of Adelaide, Adelaide, Australia. Atlas: 3D Analogue Modelling of Extensional Fault Systems Plus Field Applications (1995), published by the University of Adelaide, et al., included his Ph.D. research.

Dr. Ivan Deshenenkov is a Geologist with the Exploration Technical Services Department. He joined Saudi Aramco in 2013 with over 9 years of petrophysical experience in both service companies and exploration and production companies in Russia, the U.S. and France, specializing in petrophysics, rock physics, digital rock physics and special core analysis.

Ivan holds several patents and has authored more than 30 technical papers. During his career, he has received several awards, including the Russian President Grant, the Society of Petroleum Engineers' (SPE) STAR Fellowship and the American Association of Petroleum Geologists' (AAPG) Gustavus E. Archie Memorial Grant for research work.

He is a member of AAPG, the European Association of Geoscientists and Engineers (EAGE) and the Dhahran Geosciences Society (DGS).

In 2013, Ivan received his Ph.D. degree (with honors) in Petrophysics and Petroleum Engineering, with a concentration in capillary pressures, relative permeability analysis and reservoir production forecasting, from Gubkin Russian State University of Oil and Gas, Moscow, Russia.

Saudi Arabia oil & gas

www.saudiarabiaoilandgas.com

Contribute to Saudi Arabia Oil & Gas during 2017

EPRasheed is looking for editorial submissions on the topics outlined in the editorial calendar. This can provide your company with the opportunity to communicate EP technology to the wider oil and gas community.

Please send abstracts or ideas for editorial to **wajid.rasheed@eprasheed.com**

Preference is given to articles that are Oil Company co-authored, peer reviewed or those based on Academic research.

Editorial 2017 Calendar

Jan/Feb	Mar/Apr	May/Jun	Jul/Aug	Sep/Oct	Nov/Dec
Ad Closing: 3 Jan 2017 **Materials Closing:** 10 Jan 2017	**Ad Closing:** 3 Feb 2017 **Materials Closing:** 10 Feb 2017	**Ad Closing:** 7 April 2017 **Materials Closing:** 14 April 2017	**Ad Closing:** 7 July 2017 **Materials Closing:** 14 July 2017	**Ad Closing:** 18 August 2017 **Materials Closing:** 25 August 2017	**Ad Closing:** 6 October 2017 **Materials Closing:** 13 October 2017
Issue 48 *'Deep Diagnostics'*	**Issue 49** *'Embracing the Vision Towards Energy Prosperity'*	**Issue 50** *'KSA Upstream Research & Development"*	**Issue 51** *'Red Sea Challenges'*	**Issue 52** *'Offshore Gas'*	**Issue 53** *'Maximising Sweep Efficiency'*
• Deep Reading Technology Integrated with Inflow Control Devices • Crosswell Electromagnetic Induction • Reservoir Stress Path from 4D Coupled High Resolution Geomechanics Model	• Oil Field Automation and Optimization • Extreme Reservoir Contact • Wide Azimuth • Near Surface Resolution • Technology Innovation to Secure Future of Energy Supply Middle East	• Accelerating and De-risking New Technologies • Real Time Operations • I Field • Drilling Automation • KSA Upstream Research & Development • KFUPM Techno Valley	• Deep Water Red Sea Challenges • Assessment of KSA & IOCs Gas Exploration Initiatives • Shale Gas • Tight Gas Developments • Tight Gas Technology Development	• KSA Offshore Gas Development Projects (Karan, Wasit, Arabia, etc....) • Smart Water Chemistry in Carbonate Recovery • Development of Unconventional Gas	• Maximizing Sweep Efficiency in Heterogeneous Carbonate Reservoir Using Advanced Intelligent Completion Technology • New Stimulation Technology
BONUS CIRCULATION					
	20th Middle East Oil & Gas Show and Conference 6-9 March 2017 Manama Bahrain **SPE/IADC Drilling Conference & Exhibition** 14-16 March 2017 The Hague The Netherlands **SPE-SAS Annual Technical Symposium & Exhibition** 24-27 April 2017 Dammam, Saudi Arabia	**Offshore Technology Conference** 1-4 May 2017 Houston USA **79th EAGE Conference & Exhibition** 12-15 June 2017 Paris France		**Offshore Europe** 5-8 September 2017 Aberdeen UK **SPE Annual Technical Conference and Exhibition** 9-11 October 2017 San Antonio USA	**10th International Petroleum Technology Conference** December 2017 Doha Qatar
SPECIAL PUBLICATIONS					
	** Official Saudi Magazine	* Official Technical Magazine			* Media Partner

Improve Your Production Curve the **SMART** Way

Spatial **M**apping **A**nd **R**adial **T**hru-Bore™

‘Can you see where the fractures are without running wireline?’

‘Sure. **Smart Frac®** defines fracture geometry while drilling.’

* Red ovals show fractures.